Geophysical Journal International

Geophys. J. Int. (2018) **212,** 1600–1626
Advance Access publication 2017 November 9
GJI Geodynamics and tectonics

doi: 10.1093/gji/ggx486

Evidence of recent plutonic magmatism beneath Northeast Peloponnesus (Greece) and its relationship to regional tectonics

A. Tzanis,[1] A. Efstathiou,[1] S. Chailas[1] and M. Stamatakis[2]

[1]*Section of Geophysics—Geothermy, National and Kapodestrian University of Athens, Panepistimiopoli, Zografou* 15784, *Greece.*
E-mail: atzanis@geol.uoa.gr
[2]*Section of Economic Geology and Geochemistry, National and Kapodestrian University of Athens, Panepistimiopoli, Zografou* 15784, *Greece*

Accepted 2017 November 8. Received 2017 November 6; in original form 2017 January 21

SUMMARY

This work reports evidence of recent tectonically controlled plutonic magmatism related to Neogene volcanism in a broad area of Northeast Peloponnesus (Greece) that is straddled by the Hellenic Volcanic Arc and comprises the Argolid, the Argolic and Saronic gulfs and eastern Corinthia including the province of Crommyonia at the western half of Megaris peninsula (western Attica). We assess the contemporary stress field based on formal inversion of well-constrained crustal earthquake focal mechanisms and determine that it is principally extensional and NE-SW oriented, with σ_1 strike and plunge being N64° and 77°, respectively and σ_3 strikes and plunge N210° and 10°. This generates WNW-ESE and NW-SE faults, the former being dominant in the Saronic Gulf and the latter in the Argolic. In addition, the analysis predicts E-W and N330° faults with non-trivial right- and left-lateral heave, respectively, which are consistent with the R and R′ directions of Riedel shear theory and explain a number of observed earthquake focal mechanisms and earthquake epicentre alignments. We also present a semi-quantitative analysis of observed aeromagnetic anomalies by performing numerical modelling of the radially averaged power spectrum with an efficient anomaly separation scheme based on a new type of 2-D Fourier domain filter introduced herein, the Radial Extended Meyer Window. This analysis identifies an extensive complex of magnetized rock formations buried at depths greater than 3 km which, given the geology and geotectonic setting of the area, can hardly be explained with anything other than calc-alkaline intrusions (plutons). At northeastern Corinthia and Crommyonia, this type of intrusive activity is unexceptional, mainly concentrated in the Gulf of Megara–Sousaki areas and consistent with the low-intensity, small-scale Pliocene dacitic volcanism observed therein. Conversely, large-scale elongate anomalies of E-W and N330° orientation have been identified in the Argolid, generally collocated with and delimited by extensional tectonic structures (grabens and major faults) of analogous orientation. These are interpreted to comprise calc-alkaline plutons whose placement has been controlled by the regional tectonic activity (syn-rift magmatism); their nature and origin is demonstrated with convergent evidence from deep magnetotelluric, seismological, seismic tomography and other investigations. A large number of shallow and superficial (less than 2 km) magnetic sources have also been identified; these are generated by a complex of distributed near-surface formations consisting of subvertically developing buried or extrusive volcanics and outcropping or shallow-buried ophiolitic formations (thin nappes of tectonic mélange and dismembered ophiolitic complexes). The joint analysis of the data facilitates the formulation of a tentative geotectonic model for Argolis peninsula, according to which the strain differential caused by the disparate extensional trends of the Argolic and Saronic gulfs is accommodated by right-lateral block motion associated with igneous intrusive activity at major block boundaries.

Key words: Composition and structure of the continental crust; Structure of the Earth; Magnetic anomalies: modelling and interpretation; Numerical approximations and analysis; Earthquake dynamics.

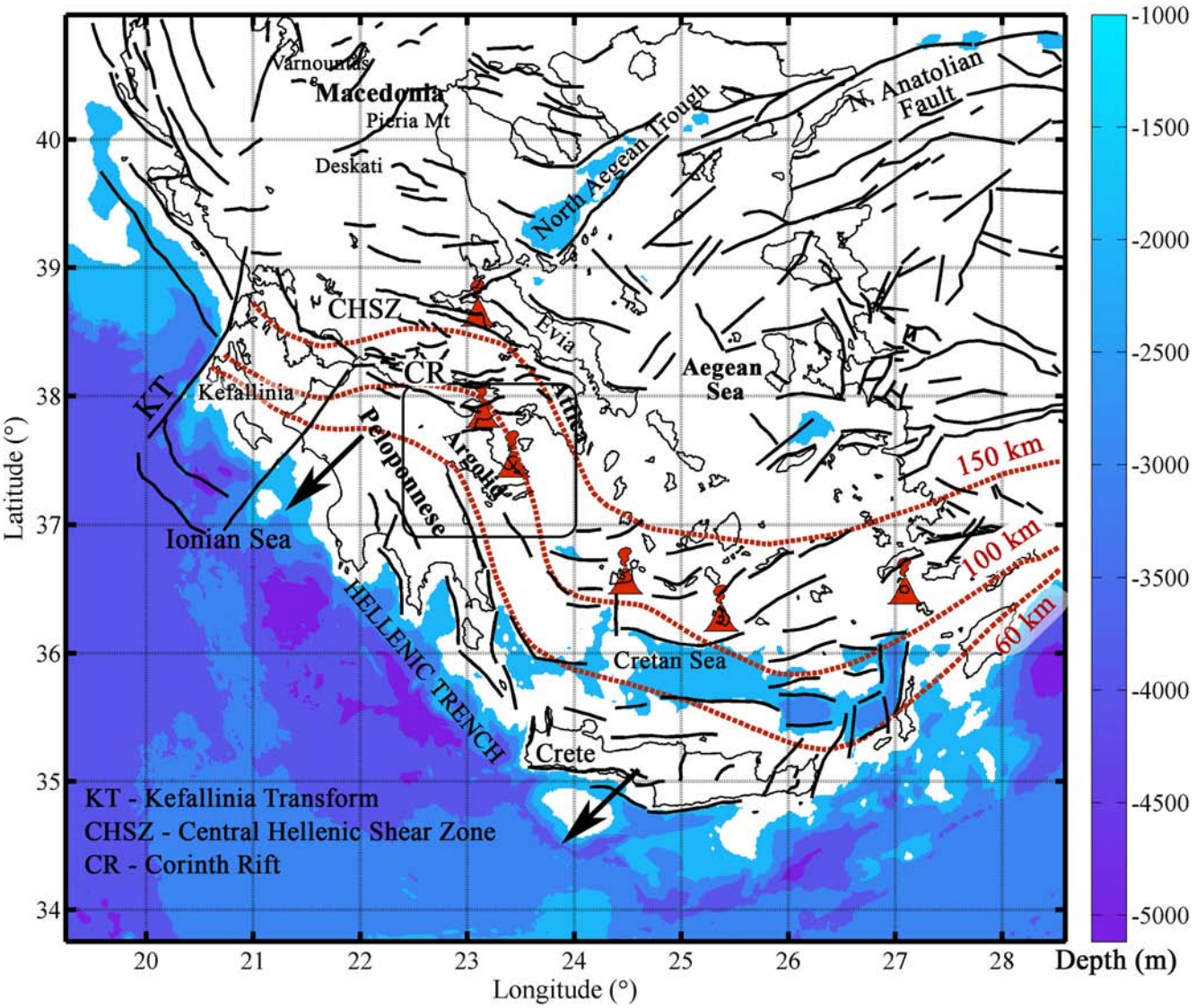

Figure 1. Synoptic depiction of the Hellenic Subduction System. The fields of the Hellenic Volcanic Arc are indicated with 'smoking volcano' symbols. The study area is outlined by the rounded rectangle between latitudes 36.9°N–38.1°N and longitudes 22.4°E–24°E. The black arrows indicate the motion of the Aegean plate relative to the African. The thick red dashed lines indicate the 60, 100 and 150 km isodepths of the subducting slab and thick black solid lines indicate active faults; both data sets were extracted from the SHARE database (Basili *et al.* 2013). Bathymetry was extracted from the ETOPO1 database (Amante & Eakins 2009).

1 INTRODUCTION

The area of NE Peloponnesus (Argolid and Corinthia) is not only geologically complex, but is also part of a fascinating contemporary geotectonic setting (Fig. 1). As will be reviewed in Section 2, it is part of the broader Corinth Rift (CR) system and is bounded by the W-E oriented Gulf of Corinth (GoC) to the north, which is the rapidly spreading core of CR, by the NW-SE oriented extensional subsystem (graben) of the Argolic Gulf and Argolic Plain to the west and by the complex extensional structures of the Saronic Gulf to the east. In addition, it is underlain by the Hellenic Subduction System (HSS) whose local geometry and influence on crustal tectonics is certainly not simple and as yet imprecisely understood. As part of this system, the Peloponnesian Northeast is straddled by the NW-SE oriented Hellenic Volcanic Arc (HVA) —also known as South Aegean Volcanic Arc— and features two known volcanic fields: the small Methana Volcanic Complex (MVC) at the east coast of the Argolid and the local-scale Sousaki solfatara at Crommyonia, near the southern margin of the GoC (Figs 1 and 2). However, with the exception of these fields, the broader CR area appears to not exhibit some type of syn-rift volcanism, a characteristic also unique among other active rift systems.

In spite of the interest it apparently presents as part of a very active rollback system with active volcanism, and by all probability due to its low seismicity rate, the Peloponnesian Northeast has rarely been the focus of specialized or trans-disciplinary research and has undeservingly not attracted as much attention as that directed to the GoC area. The pre-Alpine geology and tectonics are rather more extensively studied than their post-Alpine counterparts and contemporary crustal deformation has not been examined to an appreciable level. GPS surveys have been limited to the GoC. All but one published examples of seismological work have focused on deep structures and processes and the sole crustal seismicity study was confined to the Saronic Gulf and did not address questions about the

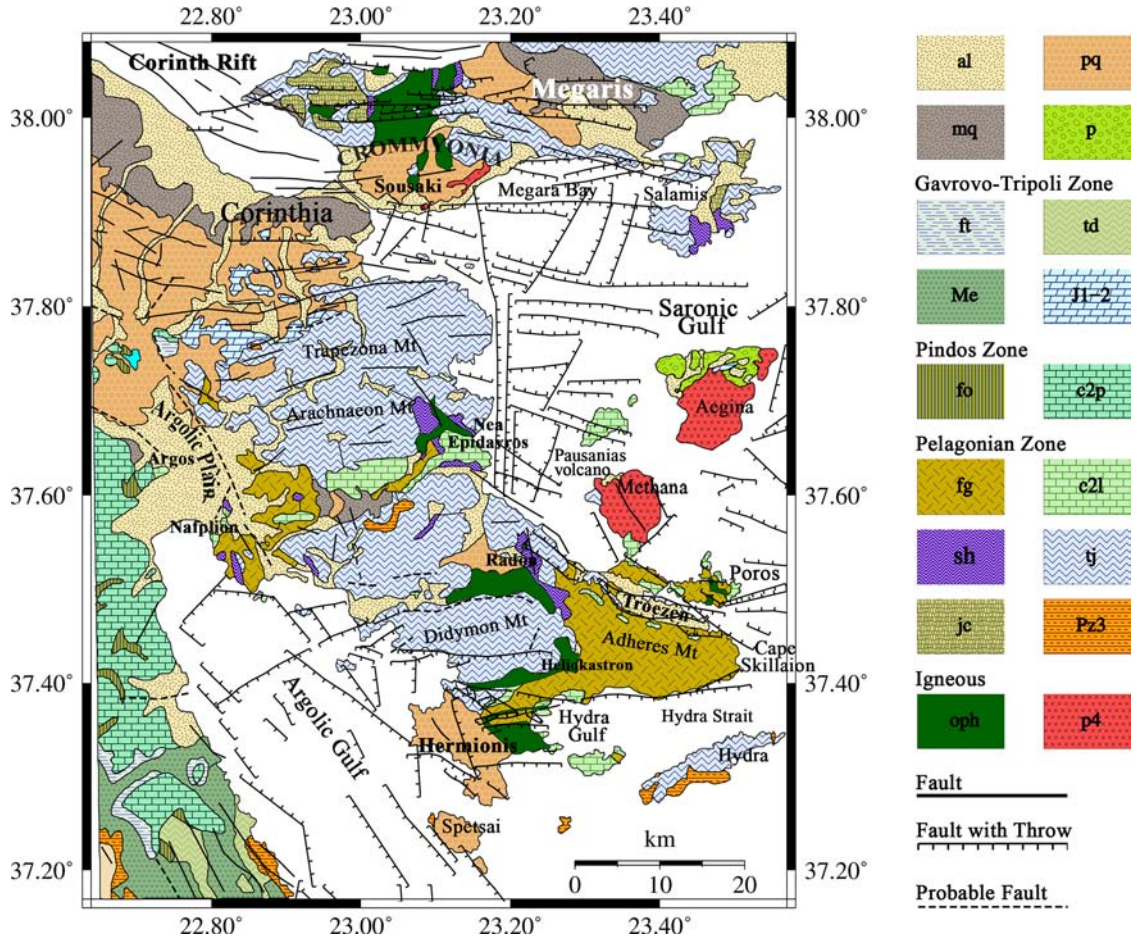

Figure 2. Geological and location map of the study area. Codenames of geological formations are as follows: *Cenozoic*: **al**, alluvial deposits; **pq**, Plio-Pleistocene lacustrine and marine sediments; **mq**, Pleistocene lacustrine and terrestrial sediments; **p**, Pliocene marine sediments. *Tripoli and Parnassus zone*: **ft**, flysch; **td**, Middle-Late Triassic dolomites; **Me**, Mesozoic–Eocene limestones and dolomites undivided; **J1–2**, Early-Middle Jurassic limestones. *Pindos zone*: **fo**, flysch; **c2p**, Late Cretaceous limestones. *Pelagonian zone*: **fg**, flysch; **c2l**, Late Cretaceous limestones; **sh**, shale-chert formation (ophiolitic-sedimentary mélange); **tj**, Triassic–Jurassic limestones (Didyma–Trapezona Formation); **jc**, Boeotian flysch; **Pz3**, various Late Palaeozoic and Permotriassic formations, unclassified. *Igneous*: **oph**, generic classification of ophiolitic rocks (generally harzburgites, serpentinites, gabbros, amphibolites, andesitic lavas in schistose serpentinine matrix); **p4**, generic classification of Quaternary calc-alkaline volcanic rocks (andesites to dacites). Fault data were collected from Papadeas (1989), Kokkalas & Aydin (2013), Papanikolaou *et al.* (1988), Vassilopoulou (1999), Skourtsos & Kranis (2009), Kranis (1999) and Stefatos *et al.* (2002). The map was created with version 5.3 of the GMT software package (Wessel *et al.* 2013).

configuration of the stress field and associated deformation modes. The primary coastal and offshore neotectonic extensional faulting structures are rather successfully mapped by marine geophysical surveys in the Argolic and Saronic gulfs, but little is actually known of the secondary and auxiliary onshore and offshore faulting modes, let alone of their causative stress field. Onshore geophysical work focusing on large- or regional-scale crustal structures has not been carried out; the possibility of past or present syn-rift magmatic activity is undetermined.

In this study, we focus on a rather broad area straddled by the northwest branch of the HVA, which includes the Argolid, the Argolic and Saronic gulfs and eastern Corinthia including the area of Crommyonia at the west of Megaris peninsula, where the Sousaki solfatara is located (Figs 1 and 2). We address questions relating to the configuration of the crustal stress field and deformation modes, as well as to the existence of (syn-rift) magmatism and its relationship to crustal deformation. To this effect, we use all available earthquake focal mechanisms and formal stress inversion in order to deduce the contemporary stress field, constrain the resulting active faulting modes and correlate them with geologically mapped faults and fault zones. We also use a well-constrained aeromagnetic data set together with an efficient magnetic anomaly separation scheme, in order to distinguish between the magnetic signatures of deep-seated and shallow-buried or superficial rock formations. Given the geotectonic setting of the area, deep-seated formations can hardly be explained with anything other than calc-alkaline intrusions (plutons). To this end, we use deep magnetotelluric, seismological, seismic tomography and other information to argue for the origin and nature of the intrusions. With these lines of evidence, it may be possible to make some progress in deducing the existence of syn-rift magmatism by correlating the geometry and location of deep-seated magnetized rocks with respect to the active extensional and trans-tensional faulting structures.

2 TECTONICS AND GEOLOGY

Section 2 provides a thorough review of the complex geodynamic tectonic and geological setting of our study area and comprises four parts. Sections 2.1 and 2.2, respectively, comprise an exposé

of the large-scale dynamics responsible for the Quaternary—Holocene calc-alkaline crustal magmatism and the tectonic framework facilitating the emplacement of these magmas. Additionally to providing geological context, this information is essential for the interpretation of the deep aeromagnetic anomaly sources. Observable magnetic anomalies can also be generated by mostly near-surface Mesozoic ophiolitic tectonic mélange, emplaced by alpine thin-skinned tectonics and further deformed by neotectonic activity**.** A large part of the work presented herein aims at separating the magnetic signatures of these profoundly different suites of rock. To this end, Section 2.3 provides an overview of the Quaternary volcanism and Section 2.4 a review of the geology and magnetic properties of the ophiolitic formations. This information is essential in understanding the context of the near-surface anomaly sources and interpreting the results of the separation exercise.

2.1 Geodynamic setting

A defining deep dynamic feature with profound influence on crustal tectonics, as well as genitor of the HVA, is the active subduction of the African oceanic crust beneath the Aegean plate HSS. The HSS exhibits changes in the rate and direction of subduction along its length (Fig. 1). At present, rapid subduction occurs along an arcuate belt of approximately 400 km between the islands of Crete to the south and Kefallinia to the NW; the front of the subduction is clearly defined by the bathymetry of the Hellenic Trench and the rate of convergence is estimated at 40 mm yr^{-1} (Clarke *et al.* 1998; McClusky *et al.* 2000).

In the vicinity of the study area, the subducting slab is NNW oriented and plunges to the E-NE. The geometry and internal structure of the slab are not uniquely determined and the isodepth contours shown in Fig. 1 are only based on one interpretation of the available data (Basili *et al.* 2013). Specifically, the subduction is associated with a Wadati–Benioff zone which, according to Papazachos *et al.* (2000), is dipping at approximately 30° from 20 to 100 km depth and at approximately 45° from 100 to 150 km. These authors locate the 100 km isodepth, hence the inflection of the slab, beneath an imaginary line passing through Hermionis and the Isthmus of Corinth, which is offset by approximately 25 km to the west of the 100 km isodepth depicted in Fig. 1. By mapping hypocentres and focal plane mechanisms of subcrustal earthquakes, Hatzfeld *et al.* (1989) place the inflection at a depth of 50–60 km, at a zone consistent with the geographical location and orientation of the Argolic Gulf; they also place the 100 km isodepth at a zone consistent with the geographical location of the HVA and MVC at the NE coast of the Argolid. This is compatible with the depths at which eclogite facies metamorphism drives water into the mantle wedge and initiates the generation of andesitic magmas and arc volcanism (e.g. Grove *et al.* 2006, and references therein). No inflection is detected in the 2-D tomographic analysis of Suckale *et al.* (2009) who image a rather thin (∼10 km) slab plunging at 21° to a depth of approximately 90 km beneath the Crommyonian volcanic field (see Figs 1 and 2). This is not consistent with earthquake activity at depths greater than 100 km beneath the Saronic Gulf and Attica (see Section 5 for details). It is also not consistent with the tomographic imaging of Sachpazi *et al.* (2016), who identify an inflection at approximately 60 km beneath the Argolic Plain (Fig. 2). These authors also detect segmentation in the slab, caused by along-dip faults in a manner suggestive of mechanical coupling with the overriding (Aegean) plate that strongly influences the deformation of the latter.

The thickness of the upper (overriding) plate is a factor significantly influencing the manifestation and type of crustal magmatism; it is also not uniquely determined in our study area. For example, Drakatos *et al.* (2005) assert that it is limited to about 20 km and attribute their observation to the extensional thinning and the emergence of the mantle material which, they assert, reaches up to the depth of 12 km, consistently with the estimation of the depth to the Curie isotherm given by Tselentis (1991). On the other hand, Sachpazi *et al.* (2007), Suckale *et al.* (2009) and others, place the upper (Aegean) plate Moho at approximately 37 km beneath the west coast of the Argolic Gulf and 30 km beneath the western Saronic. This indicates significant thinning of the Aegean crust between east Peloponnesus and the Saronic Gulf, initiating approximately beneath the Argolic Gulf and Plain. The deep magnetotelluric study of Galanopoulos *et al.* (2005) detects a 'wall' of relatively conductive material beneath an onshore location a few kilometres north of the head of the Argolic Gulf, which appears to transgress the base of the Aegean plate crust and spread sideways beneath the Peloponnesus. As will be argued in Section 5, this points to partial melting in the upper mantle and subducting crust and may be related to the inflection of the slab and the thinning of the Aegean plate crust. All the above evidence indicate that the inception and evolution of the Argolic Gulf may be related to deep-rooted processes and may comprise a major component of the geotectonic setting of the study area. Analogous and significantly broader columns of conductive material appear to upwell from the subducting slab at a depth of approximately 100 km and rise through the mantle wedge to the base of the crust beneath Crommyonia: this is direct manifestation of partial melting associated with the HVA.

2.2 Regional tectonics

In the Aegean plate, the area between the dextral Kefallinia Transform (Fig. 1) and the Aegean Sea defines the Central Hellenic Shear Zone of trans-tensional deformation, with displacement rates of the order of 25 mm yr^{-1} (Peter *et al.* 1998; Kahle *et al.* 2000). Within this zone of active extension lies the rapidly spreading CR: this is a young W-E oriented extensional graben developing in a compressional regime of continental collision and manifesting high complexity and increased seismicity and deformation rates: an NNW-SSE oriented extensional stress field generates W-E normal faults and accommodates the strain produced by the dextral shear motions of North Anatolian/North Aegean fault systems to the E-NE and the Kefallinia Transform to the west. The most active contemporary feature of the CR is the W-E oriented GoC, described as a composite asymmetric graben (Stefatos *et al.* 2002) with varying geometry along strike (Sachpazi *et al.* 2003; McNeill *et al.* 2005). Extensive geological studies of the GoC fault system (e.g. Doutsos & Piper 1990; De Martini *et al.* 2004; Flotté *et al.* 2005; McNeil *et al.* 2005), earthquake focal mechanisms (e.g. Rigo *et al.* 1996) and geodetic investigations (e.g. Billiris *et al.* 1991; Briole *et al.* 2000; Avallone *et al.* 2004), have shown that the GoC is subjected to N-S extension of 1.0–1.6 cm yr^{-1}, with higher rates observed at the west and lower rates at the centre of the rift. Armijo *et al.* (1996) suggest that 50 per cent to 75 per cent of the total extension rate (∼0.7 cm yr^{-1}) is accommodated through high-angle normal faulting, although this may be an overestimation (Westaway 2002). The W-E active faults of the CR appear to extend eastwards in a diffuse zone

through central Greece (e.g. Goldsworthy & Jackson 2001). Skourtsos & Kranis (2009) have found extensional structures with geometrical and kinematic characteristics analogous to those of known GoC faults as far south as the northern flanks of Mt Mainalon, (approximately 37.7°N), about 30 km to the west of our study area. It is also possible that the evolution of the CR is decorated with episodic-type accelerated deformation events, presumably associated with deep-seated interactions between the southward-moving Aegean continental forearc and the subducting African oceanic plate (Leeder *et al.* 2012).

The areas of the Argolid and the Argolic and Saronic Gulfs are closely related to the CR system. However, contrary to the exhaustively investigated GoC, these areas have not been as thoroughly studied. The Argolis peninsula is flanked by the Argolic Gulf to the west and the Saronic Gulf to the east (Fig. 2). According to Papanikolaou *et al.* (1988), the Argolic Gulf is a symmetric basin of NW-SE orientation and during the Pliocene–Early Pleistocene formed a channel joining the south Aegean Sea with the GoC and isolating the peninsula from the rest of the Peloponnese. The main faults there have NW-SE and rarely ENE-WSW orientation. Van Andel *et al.* (1993) characterize the Argolic Gulf as a half-graben, in which the eastern marginal faults are a brittle response to downwarping. They also assert that it is an active structure with Holocene subsidence rates along its western margin increasing from about 50 cm ka^{-1} near Argos to 100 cm ka^{-1} near the mouth of the Gulf, and along its eastern margin from zero near Nafplion to 150 cm ka^{-1} in the vicinity of Spetsai Island. Seismological evidence by Drakatos *et al.* (2005) indicate that the Saronic Gulf is divided in two basins by a central platform which, they conjecture, is the offshore extension of a large thrust belt dominating the adjacent onshore areas of Attica. The western basin is characterized by higher seismic activity and is furthermore distinguished into a northern and a southern block by a seismologically well-defined W-E rupture zone which is located between Aegina and Salamis islands, extends onshore into the Peloponnese and is interpreted to comprise an extension of the CR faulting system.

A line of evidence suggests that the expression of normal faulting changes from W-E at the GoC to WNW-ESE in Saronic (N110° on average, Papanikolaou *et al.* 1988) and to NW-SE at the Cyclades (S. Aegean) in two discrete steps (e.g. Papanikolaou & Lozios 1990). This indicates a corresponding rotation of the σ_3 principal stress axis. Based on their analysis of the surrounding areas and a single focal mechanism of the $M_w = 5.2$ event of 1968 July 04 by Ritsema (1974), Kiratzi & Louvari (2003) suggest that in the Saronic, the extensional field has NNE-SSW orientation. Their conclusion is corroborated by four mechanisms of small crustal earthquakes located at the Argolid and published by Hatzfeld *et al.* (1993).

Whereas the main deformation mode in the Argolic and Saronic gulfs appears to be NW-SE extension, such faults can only be observed at the NE and SW coasts of Argolis peninsula, corresponding to the NE-dipping boundary faults of the Saronic and the SW-dipping boundary faults of the Argolic gulfs. As summarized in Vassilopoulou (1999, 2010, and references therein), within the peninsula the main orientation of major terrain features and morphological discontinuities is W-E and the orientation of neotectonic faulting structures and zones is mainly WNW- ESE to W-E. These structures form a series of local horsts and grabens with particular reference to the Mt Adheres area at the SE and Hermionis peninsula at the SW; they are most active at the south and SE, where they contribute to the formation of the tectonic basin of Hydra Gulf and Strait, as well as at the SW, towards Kranidi and the Argolic Gulf (Fig. 2).

2.3 Quaternary volcanism

Quaternary to contemporary volcanism is manifest in the MVC which is located at the NE coast of Argolis peninsula, as well as in the Sousaki solfatara field located at the Crommyonia province of northeastern Corinthia (terminus of the HVA). The Sousaki solfatara (e.g. Francalanci *et al.* 2005, and reference therein) is the relic of a small volcanic field that used to be active between 4 and 2.3 Ma ago (Late Pliocene–Early Quaternary). The observable volcanic outcrops are generally small (total volume less than 1 km^3); they are distributed over a large area and consist of dacitic lava domes and associated lava flows. Vent distribution and edifice shapes exhibit W-E and NW-SE anisotropy and appear to be controlled by tectonic lineaments of analogous orientation, related to the CR system. Explosive activity concurrent with the emplacement of lava domes is evident by layers of tuffs and tuffites found in lacustrine deposits of the same age as the volcanic outcrops. The Sousaki area today hosts a low-temperature geothermal field (up to 80 °C) and weak fumarolic activity emitting low-temperature gasses (30–40 °C). Post-volcanic hydrothermal activity and continuous CO_2-rich outgassing have resulted in pervasive alteration of the igneous rocks (serpentinites and dacites).

The Methana volcano comprises an ensemble of domes dated from 0.9 million to a few thousand years BCE, although activity may have begun during the Late Pliocene (Dietrich & Gaitanakis 1995; Pe-Piper & Piper 2002, 2013; Smet 2014). The most recent eruptive episode has been described by Strabo and has taken place in approximately 230 BCE. Peripheral to the volcano magmatic activity appears both on- and offshore. Evidence of onshore activity is found in Poros Island, in the form of a small (*ca.* 1 km^2) andesitic outcrop with composition similar to that of the Aegina volcanics (Mitropoulos 1987; Francalanci *et al.* 2005). Evidence of offshore activity has been identified a few kilometres to the NW of Methana peninsula, where andesitic lavas have been dredged, having an age of approximately 1 Ma as estimated on the basis of the thickness of the sedimentary cover (Papanikolaou *et al.* 1988). This is the site of the Pausanias submarine volcano, where short-lived extrusive activity has also taken place in 1700 CE. Contemporary activity in the MVC is limited to geothermal springs along the coastline, usually at locations associated with faulting (e.g. Dotsika *et al.* 2010). In addition, there is one thermal spring in the area of Hermioni, with temperatures of the order of 20–40 °C. The heat flow map published by the Institute of Geological and Mineral Exploration (IGME, Taktikos 2001) indicates high rates (70–150 mW m^{-2}) at Methana peninsula, intermediate rates (50–70 mW m^{-2}) at south Argolis, and relatively low rates (30–50 mW m^{-2}) at the north and central Argolis.

2.4 Pre-Alpine ultramafic rocks

The study area has a complex geological structure comprising small outcrops of pre-Alpine formations mainly at the south (e.g. Hydra Island), various alpine series of the Pelagonian zone, small outcrops of Mesozoic limestones of the Parnassus zone around (37.8°N, 22.8°E) and Plio-Pleiostocene sediments related to the CR at the north (Fig. 2). The stratigraphy, sequence and (tectonic) placement of these formations are of no consequence to the present analysis and will not be elaborated. The study area is also characterized by

the presence of ultramafic formations (ophiolitic mélange) which are very important. These appear as patches outcropping along a broad N-S zone from Crommyonia (Megaris peninsula) to South Argolid (Hermionis area).

The Crommyonian (or Gerania) ophiolites have generally not been extensively studied. Recent work (Kaplanis *et al.* 2013) indicates that they have been emplaced by thin-skinned thrusting over the Pelagonian margin during the Early Cretaceous (Eohellenic tectonic phase). This process has dismembered the ophiolitic complex so that the Crommyonian outcrop is essentially a (thin) nappe consisting mainly of serpentinized harzburgites. The magnetic susceptibility of the outcrop was measured *in situ* at 10 different locations and varies between 6×10^{-3} and 15×10^{-3}, with a mean of 11×10^{-3} and a median of 11.55×10^{-3} (Efstathiou 2011). It follows that magnetic anomalies would be significant only if the outcrop was massive and of large depth extent. The ophiolites are closely related to the Boeotian flysch which is essentially a mélange consisting of ophiolite-derived turbidites.

The ophiolitic outcrops of the Argolid have attracted considerable attention. According to Gaitanakis & Photiades (1989), there are three ophiolitic units. The lower unit is a Late Jurassic ophiolitic-sedimentary mélange thrusted on Late Triassic–Early Jurassic carbonates (Didyma–Trapezona formation). The intermediate unit comprises a series of dolerites, ultramafic lavas and cherts, formed by superficial thin-skinned overthrusting of oceanic crust onto the lower unit during the Late Jurassic–Early Cretaceous (Eohellenic tectonic phase). Finally, the upper unit is an ophiolitic tectonic mélange (harzburgites, serpentinites, gabbros, amphibolites, andesitic lavas in a schistose serpentinine matrix), thrusted on Late Cretaceous–Ypresian carbonates at the end of the Eocene. According to Gaitanakis & Photiades (1991, 1993), the most conspicuous and massive ophiolitic formations are those of the upper unit which is also characterized by suprasubduction related geochemical signature as well as extensive alteration and static greenschist metamorphism. Gaitanakis & Photiades (1991, 1993) posit that in the SW Argolid, the ophiolitic mélange enriched with basalt fragments was thrusted on the crystalline basement (volcano sedimentary sequence) during the Late Jurassic and not on a carbonate platform as in the north and central Argolid. All ophiolitic formations are serpentinized and more or less weathered, altered and fragmented. These processes are detrimental to the magnetic susceptibility which varies from 0.02×10^{-3} to 0.06×10^{-3} in the radiolarites and the matrix of the mélange, to 0.1×10^{-3}–10×10^{-3} in heavily weathered/altered samples and to 20×10^{-3}–36×10^{-3} in healthier samples (Efstathiou 2011). Such susceptibilities indicate that the ophiolitic formations should not generate large amplitude magnetic anomalies, unless they are massive and of great depth extent.

3 CONTEMPORARY STRESS FIELD AND SEISMOTECTONICS

Geological and tectonic mapping has not yet produced field evidence of the contemporary stress field in the study area, while reliable earthquake focal mechanisms have been rare until year 2002. As of that time, the establishment of the expanded Hellenic Unified Seismological Network (HUSN) and the installation of the ATHENET network by the University of Athens (as part of its contribution to the HUSN), have enabled continuous monitoring of the area with a sustainable detection threshold of at least $M \approx 1.5$ (e.g. D'Alessandro *et al.* 2011), as well as the determination of reliable focal mechanisms with advanced techniques based on full-waveform inversion. Table 1 is a list of all hitherto known and well-constrained focal mechanisms of *crustal* ($D < 30$ km) earthquakes located in the broader study area. Fig. 3 illustrates the equal-area (Schmidt) projections of post-1990 mechanisms, that is, only those determined by full-waveform inversion techniques. Quite apparently, the number, diversity, geographical and magnitude distribution of the latter 33 mechanisms are adequate to warrant estimation of the crustal stress field by inversion, at least to a first approximation.

Let the stress field be defined in the standard geological/geophysical sense with $\sigma_1 > \sigma_2 > \sigma_3 > 0$ representing the principal stress axes. Then, the relative magnitude and orientation of the stress axes can be computed from focal mechanisms by *formal inversion*, that is, by finding the stress tensor that optimally reproduces the observed focal mechanisms. The stress field inversion method implemented herein is the SATSI algorithm of Hardebeck & Michael (2006), as redesigned and recast into the MSATSI software package by Martínez-Garzón *et al.* (2014). In fact, SATSI is an upgraded version of the method of Michael (1984, 1987) and uses a bootstrap resampling method to calculate misfit and home into the optimal solution. According to Hardebeck & Hauksson (2001), this approach is more accurate for noisy data sets and provides a more appropriate estimate of uncertainty. The inversion also returns a measure of the misfit between the optimal (best fit) solution and the data; this is given by the angle $\bar{\beta}$ which is the mean of the angles β formed between the calculated slip vector from stress tensor inversion and the observed slip vector from fault plane solutions. A synthetic control study showed that the amount of heterogeneity in the stress field could be characterized by means of $\bar{\beta}$: for focal mechanism data with errors of the order 10°–30°, $\bar{\beta}$ varies in the range 30°–45° when the spatially uniform and variable parts of the stress field have equal sizes (Michael 1991). Thus, misfit angles significantly lower that these values can be taken to indicate satisfactory solutions and approximately homogeneous stress fields.

Conditions for the results of formal inversion to be meaningful are: (i) the stress should be uniform in the study area, at least during the interval in which the data were acquired; (ii) the earthquakes under consideration should be shear dislocations on pre-existing faults; (iii) similar shear stress magnitude should be present at each fault and (iv) the slip should occur in the direction of the resolved shear stress on the fault plane. Accordingly, the inversion was carried out on the basis of 22 post-2002 events with moment magnitudes between 3.8 and 4.9 and yielded a misfit $\bar{\beta} = 18.6 \pm 15.7$. This is not exceptional but it is based on more than 15 well-constrained single events in close geographic proximity and with a misfit of less than 20° can be classified as borderline between Quality A and B, according to the ranking scheme of Zoback & Zoback (1989, 1991) as refined by Sperner *et al.* (2003) and used by World Stress Map Project. A graphical representation of the expected crustal stress result is shown in Fig. 4: the principal compression axis σ_1 is oriented at N64° and plunges at 77° (open square), while the principal extensional axis σ_3 is oriented at N210° and plunges at 10° (open circle). The stress field is mainly extensional, NNE-SSW oriented and overall homogeneous. The 'typical' focal mechanism generated by this field is shown with thick black lines and a schematic depiction of the faulting pattern predicted by Riedel's shear theory is also superimposed.

According to the results above, the expected principal direction of normal faulting is WNW-ESE (approximately N290°) for northeasterly dipping faults and NW-SE (approximately N130°) for southwesterly dipping faults. The former is spectacularly manifested in the hanging cliffs of the northern coast of Argolis peninsula, as well as in identically oriented normal faults mapped by

Table 1. All known crustal ($D < 30$ km) focal mechanisms at the broader area of the Argolid.

					Location (Source)			ISC location							
Year	Month	Day	hr	min	Lon.	Lat.	D	Lon.	Lat.	D	M_w	Strike	Dip	Rake	Source
1968	7	4	21	47	23.20	37.7	15	23.23	37.76	20	5.5	97	58	−65	RTS
1988	7	14	17	08	23.03	37.71	17	NA	NA	NA	2.0	49	70	1	HATZ
1988	7	14	20	40	23.01	37.70	13	NA	NA		2.0	250	49	89	HATZ
1988	8	17	12	08	23.11	37.72	17	NA	NA		2.5	205	30	−90	HATZ
1988	8	18	12	00	23.08	37.73	11	NA	NA		2.4	199	60	−90	HATZ
1999	9	7	11	56	23.64	37.87	15	23.582	38.122	9.4	5.9	116	39	−81	GCMT
2002	1	24	3	59	22.81	38.06	5	NA	NA	NA	3.5	67	80	−86	KONST
2002	9	7	20	22	22.85	37.10	13.0	22.975	37.172	17.8	3.8	76	84	−19	KONST
2002	11	23	1	14	22.56	37.98	12.0	22.642	38.031	22.1	3.8	62	66	−85	KONST
2004	2	17	15	56	22.63	38.07	5.0	22.657	38.108	20	3.9	127	37	−50	KONST
2006	9	10	4	40	22.70	38.10	5.0	22.769	38.099	14.4	4.0	98	24	−50	KONST
2006	11	16	18	50	23.10	36.96	8.0	23.231	36.960	10.5	3.6	67	26	−6	KONST
2008	1	29	15	16	23.517	37.643	8.0	23.437	37.604	13.4	4.2	109	52	−106	UoA
2008	4	14	12	25	23.2593	37.854	12.0	NA	NA	NA	3.4	85	48	−62	UoA
2008	8	3	13	01	23.4911	37.3948	10.0	23.486	37.332	9.1	3.9	118	70	−74	UoA
2008	9	18	07	02	23.7326	37.066	12.0	23.704	37.0398	9.7	3.8	120	65	−80	UoA
2008	9	30	0	43	23.2894	38.1139	8	NA	NA	NA	3.7	108	62	−90	UoA
2009	3	6	1	45	22.9296	37.5797	5.0	22.9302	37.6073	14.4	3.8	106	79	−102	UoA
2009	5	17	11	59	22.69	38.13	6.0	22.6944	38.1194	13.9	4.6	103	41	−89	AUTH
2009	9	2	9	35	23.32	38.11	5.0	23.2739	38.1082	9.4	4.0	106	34	−74	NOA
2010	12	14	13	58	22.83	38.08	16.0	22.7868	38.0608	13.7	3.9	133	84	−7	NOA
2011	1	31	17	23	22.70	37.87	17.0	22.7131	37.8784	16.3	3.5	160	60	−31	NOA
2011	10	24	9	24	23.509	37.609	9.0	23.5118	37.6070	12.9	3.5	118	31	−115	NOA
2011	12	08	20	59	23.5252	38.0838	7.0	23.5121	38.0980	10.5	3.6	113	53	−73	NOA
2012	2	17	8	5	23.044	37.865	14.0	23.0322	37.8503	11.4	4.1	126	45	−85	UoA
2012	9	22	3	52	22.7377	38.086	25.0	NA	NA	NA	4.9	102	70	−98	NOA
2012	12	4	18	59	23.100	36.9253	10.0	NA	NA	NA	4.3	171	46	−71	NOA
2012	12	5	3	27	23.0605	36.9232	8.0	NA	NA	NA	3.5	178	56	−60	NOA
2012	12	6	17	48	23.1094	36.9453	13.0	NA	NA	NA	4.4	171	51	−71	NOA
2012	12	9	1	23	22.5970	37.9278	12.0	NA	NA	NA	4.0	97	31	−95	UoA
2012	12	13	6	36	23.3267	37.5160	12.0	NA	NA	NA	3.4	77	79	−171	NOA
2013	6	4	1	56	23.9645	37.9612	21.0	NA	NA	NA	4.0	125	33	−83	NOA
2013	11	27	14	21	23.0101	37.3418	20.0	NA	NA	NA	4.3	144	88	−96	UoA
2014	4	10	17	40	22.6132	37.9257	10.0	NA	NA	NA	3.5	99	45	−91	NOA
2014	6	28	19	9	22.8515	37.4625	14.0	NA	NA	NA	3.7	86	81	−143	NOA
2014	9	14	22	41	23.0888	37.6978	13.0	NA	NA	NA	3.9	161	80	−111	NOA
2014	9	16	41	40	23.0037	37.1812	21.0	NA	NA	NA	3.9	183	77	−129	NOA
2014	9	18	24	25	23.0888	37.6978	13.0	NA	NA	NA	3.8	123	57	−106	NOA

Notes: Data sources are as follows. RTS: Ritsema (1974); HATZ: Hatzfeld *et al.* (1993); CGMT: Global Centroid Moment Tensor Catalogue, http://www.globalcmt.org; KONST: Konstantinou *et al.* (2010); UoA: Laboratory of Seismology, University of Athens, http://dggsl.geol.uoa.gr; NOA: Institute of Geodynamics, National Observatory of Athens, http://bbnet.gein.noa.gr/HL and AUTH: Seismological Laboratory, University of Thessaloniki.

Papanikolaou *et al.* (1988) within the Saronic Gulf. This result is also consistent with the findings of Papanikolaou & Lozios (1990), while Drakatos *et al.* (2005) have mapped a similarly oriented lineament of crustal earthquake foci between Methana peninsula and Aegina Island, collocated with faulting structures mapped by Papanikolaou *et al.* (1988). The latter faulting direction is observed mainly offshore, along the northern margin of the Argolic, between Spetsai Island and the head of the gulf (Papanikolaou *et al.* 1988; Van Andel *et al.* 1993). It is also inferred to extend onshore, flanking the eastern margin of the Argolic Plain. In addition, the results predict the existence of W-E faults consistent with the synthetic (dextral) R-shear direction of Riedel's shear theory and NW-SE (approximately N330°) faults consistent with the antithetic (sinistral) R´-shear direction. The configuration of the stress field allows for a small ENE-WSW compressional component which may easily account for local-scale faulting with significant heave. Indeed, active, oblique-normal (trans-tensional) faulting consistent with the expected R and R´ directions can be seen to exist in a few focal mechanisms of small earthquakes observed in the southern Argolid and the Argolic Gulf (Table 1 and Fig. 3). More detailed analysis of the significance of the results—and the significance of lateral-slip faulting in particular—is deferred to Section 5 (Discussion and Conclusions), where seismotectonic, aeromagnetic and other geological evidence is jointly interpreted. The above stress configuration requires the existence of crustal-scale WSW-ENE (N70°–N80°) regional shearing deformation which, we assume, is accommodated in the background SW-ward translation of the Aegean plate. It is also worth mentioning that this orientation is parallel to the orientation of the WSW-ENE shear structures investigated in central Greece by Tzanis *et al.* (2010), indicating that it may be part of a broader deformation pattern.

4 AEROMAGNETIC DATA ANALYSIS

4.1 Aeromagnetic data

The aeromagnetic data used herein have been extracted from the recently (re)compiled aeromagnetic map of Greece (Chailas

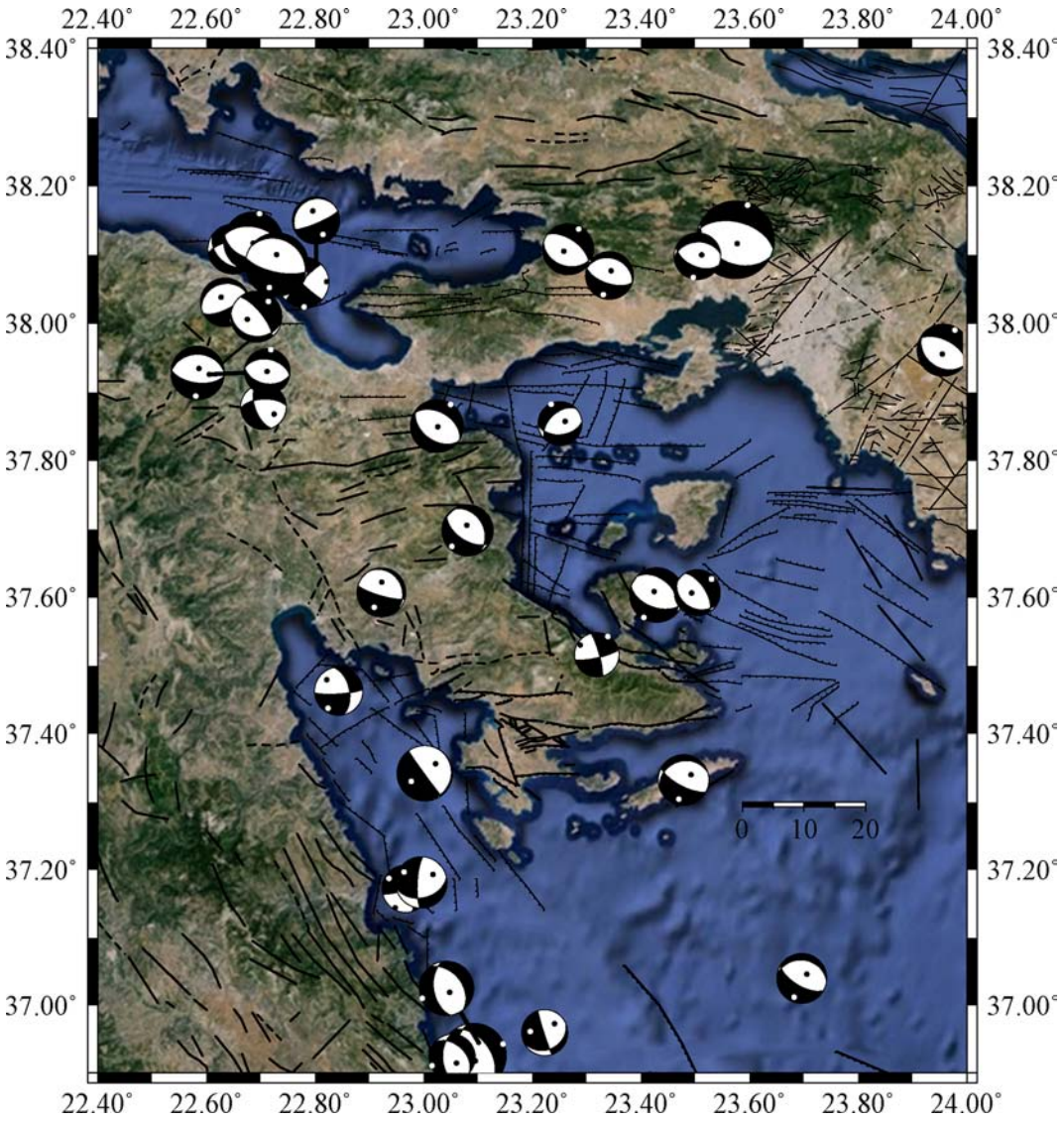

Figure 3. Fault traces and focal mechanisms of post-1990 crustal earthquakes in the broader area of the Argolid; the beach balls of pre-2012 mechanisms are plotted on their ISC primary coordinates; when available, see Table 1 for details. The map was created with version 5.3 of the GMT software package (Wessel *et al.* 2013).

et al. 2010) as augmented by Efstathiou (2011). These authors attempted to generate a unified, homogeneous and common-referenced aeromagnetic map of Greece, out of the fragmentary information existing in a multitude of 1:50 000 scale maps produced by different contractors for IGME. With respect to the study area, the compilation was based on the 1:50 000 map series produced by Hunting Geology and Geophysics Ltd for areas C3 (Eastern Central Greece) and D2 (Central Peloponnesus). Hunting has generally used a measurement spacing of 200–250 m along track and has always flown in a NE-SW direction (approximately N45°), but at different ground clearances (GC) and track densities, depending on the topography: Area C3 was measured at a nominal GC of 300 m above ground level and nominal distance of 800 m between tracks; Area D2 was measured at a nominal GC of 2000 m above mean seal level and a nominal distance of 1000 m between tracks. In both cases, connection lines were flown in a SW-NE direction and 10 km spacing between tracks.

The original 1:50 000 map sheets were converted to high-resolution raster images and digitized to vector form in image coordinates. Using the corners of the map sheets as control points, the image coordinates were geo-located and transformed to Cartesian in the UTM projection. The digitized data were finally interpolated to a rectangular grid with a uniform spacing of 250 m, so as to generate Digital Aeromagnetic Anomaly Models (DAAM) for Areas C3 and D2, respectively. The two DAAMs were subsequently 'homogenized' by reference to a common clearance AGL. Because the DAAM of Area C3 is by far the major source of data, we have chosen to downward continue the DAAM of Area D2 to a constant clearance of 300 m AGL. This is an exercise in field continuation between arbitrary surfaces and has been carried out with the efficient equivalent sources method of Xia *et al.* (1993). Details of the procedure can be found in Chailas *et al.* (2010). The DAAM of Area C3 and the downward-continued DAAM of Area D2 were collated to generate the aeromagnetic anomaly map shown in Fig. 5(a), which was next reduced to the North Pole for subsequent analysis (RTP-DAAM, see Fig. 5b).

As is evident in Fig. 5(a), the suture between Areas C3 and D2 is not seamless and can be identified in the SW quadrant of

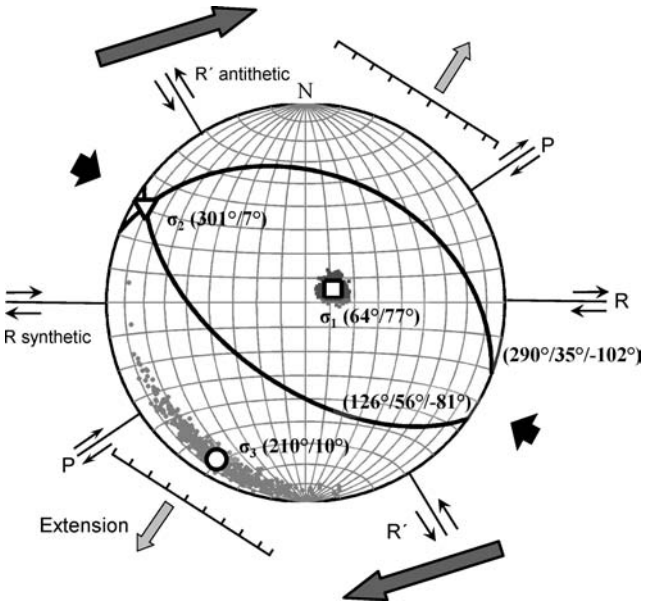

Figure 4. Schmidt projection of the stress field obtained by inversion of 22 post-2002 mechanisms with M_w between 3.8 and 4.9. Grey squares and circles indicate estimates produced by bootstrap resampling and the expanse of the 95 per cent confidence area for σ_1 and σ_3, respectively. The 'typical' expected faulting mechanisms and the schematics of the faulting pattern predicted by Riedel shear theory are also projected.

the DAAM, as well as between Easting 650–660 and Northing 670–680. The offset has variable amplitude and is presumably generated by systemic factors such as leveling error, raw data processing and imperfect continuation. One may also observe flight-line artefacts (leveling error) appearing as lineation or striation at an azimuth of N45°. These flaws are inherited from the original aeromagnetic map and are still present in the RTP-DAAM, although flight-line artefacts are not clearly seen in Fig. 5(b). Nevertheless, they exhibit rather low amplitudes and are highly localized in space, so that their effects should be significant only at long to very long wavenumbers, within the realm of noise. In consequence, they are not expected to have any measurable effect on the results.

4.2 General characteristics of magnetic sources

A semi-quantitative approach to the analysis and interpretation of aeromagnetic data is to study the scale and distribution of magnetized geological formations (sources) with depth and to separate, if possible, magnetic anomalies generated by ensembles of sources located at different depths. This exercise customarily implements spectral methods in the Fourier plane and specifically the analysis of the *radially averaged power spectrum* pioneered by Spector & Grant (1970). Note, however, that because offshore areas had been excluded from the original aeromagnetic survey, there are significant expanses of missing data. It is therefore necessary to condition the data in order to suppress spurious effects that would inevitably accompany Fourier transformation. This is done heuristically: the void grid nodes are assigned with a value equal to the arithmetic mean of the unified RTP-DAAM plus 5 per cent white noise. In this way, after the mean is subtracted for Fourier transformation, the missing data areas will assume the role of purely random variation at very long wavenumbers and will not interfere with the spectral structure of the geological magnetic sources. Gibbs effects and oscillatory aliases are suppressed by padding the RTP-DAAM with zeros to thrice its initial size: if the RTP-DAAM matrix is $M \times N$, the padded matrix is $3\,M \times 3\,N$.

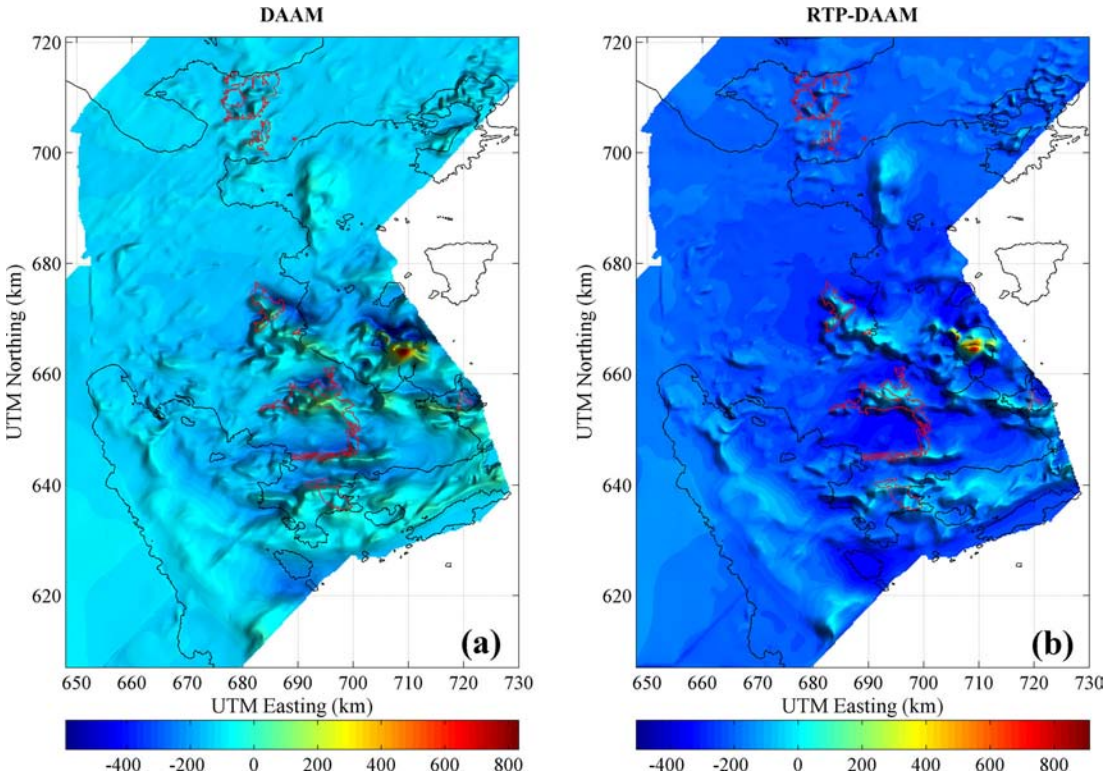

Figure 5. (a) The Digital Aeromagnetic Anomaly Map (DAAM) observed at a constant clearance of 300 m AGL. (b) Reduced to the pole (RTP) version of the DAAM. Magnetic intensity units are given in nT. Both maps are shown in shaded relief mode to facilitate visualization of small-amplitude and deep-seated anomalies. The outcrops of ophiolitic formations are also outlined. UTM northings were reduced by 3500 km so as to facilitate the display.

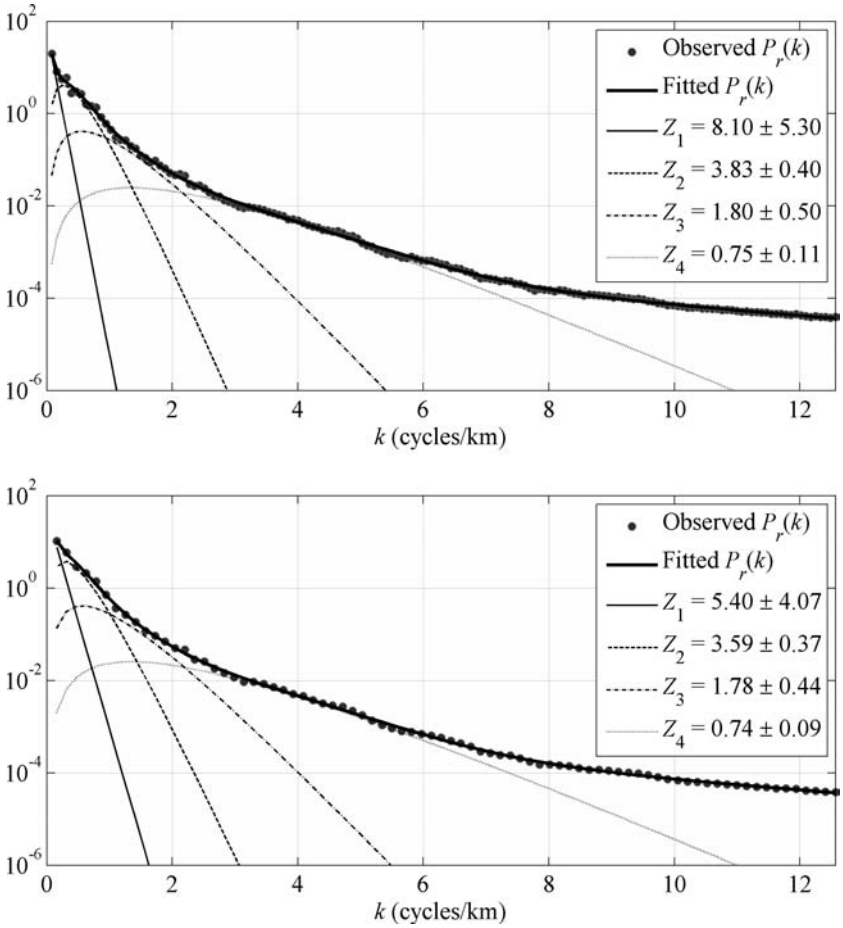

Figure 6. Modelling of two realizations of radially averaged power spectral density derived from the RTP anomaly (Fig. 5b), using different radial partitioning schemes that yield different resolutions. In both panels, solid grey circles represent the observed radial spectra and thick solid black lines the best-fitting models based on eq. (1). The other thin lines represent the responses of individual magnetic source ensembles buried at the depths Z_1–Z_4, as indicated in the legends.

Fig. 6 illustrates two realizations of the radially averaged power spectral density derived from the RTP-DAAM versus the radial wavenumber k. The radial averaging is performed by partitioning the Fourier plane into concentric circular or rectangular annuli and taking the expectation value of all power spectral realizations within each annulus. The two realizations shown in Fig. 6 were obtained with different partitioning schemes, resulting in different resolutions of the radial power spectral density. A somewhat unexpected observation in both realizations is that the basal (deepest) ensemble of magnetized structures is depth-unlimited, whereas a depth-limited layer was expected on the premise that the Curie isotherm would be elevated at the vicinity of the HVA. Notably, Tselentis (1991) has determined a Curie isotherm depth of the order of 12–15 km for the broader area of the Argolid, excluding the Saronic Gulf and the MVC. A plausible explanation, indirectly corroborated by the ensuing analysis, is that several basal sources are laterally extended and transcend the area of aeromagnetic observations, so that their floor cannot be constrained. A second important observation is the absence of conspicuous long straight line segments in the radial spectrum. The absence of transient (high-amplitude/localized) features in the RTP-DAAM, as well as high-amplitude laterally extended shallow sources and high-amplitude step-like discontinuities, precludes broad-band contamination of the wavenumber spectrum. As a consequence, the shape of the radial spectrum indicates that the sources located above the basal layer are distributed over almost all depths. This excludes spectral methods that examine isolated magnetic anomalies (e.g. Bhattacharyya & Leu 1975) and compels the implementation of methods based on statistical physics, for example, as in Spector & Grant (1970).

Although magnetic sources are not concentrated in 'layers' with distinct ceilings and floors that can be determined by standard straight line fitting methods, it is still possible to extract useful information and valuable insight. Following the formulation of Spector & Grant (1970), we approximate the radially averaged spectrum with one depth-unlimited and four depth-limited ensembles of magnetized sources using the parametric function

$$\hat{P}_r(k) = A_1 e^{-2kZ_1} + \sum_{j=2}^{5} A_j k^2 e^{-2kZ_j} + A_n \qquad (1)$$

where A_j are the ensemble strengths, Z_j are the depths to the tops of the ensembles and A_n is the noise level. We determine the parameters of eq. (1) with non-linear least squares by minimizing the loss function $\|\log P_r - \log \hat{P}_r\|^2$ subject to the constraints $A_j > 0, \quad Z_j > 0, \quad A_n > 0$. The procedure generates families of excellent best-fitting models with $R^2 > 0.99$, such as those shown in Fig. 6.

A simple inspection of Fig. 6 shows that the depth to the basal layer is inconsistently determined and is also associated with large confidence intervals. In fact, the determinability of the strength and depth to the basal layer is very sensitive to the averaging scheme with which the radial spectrum is calculated; this affects the

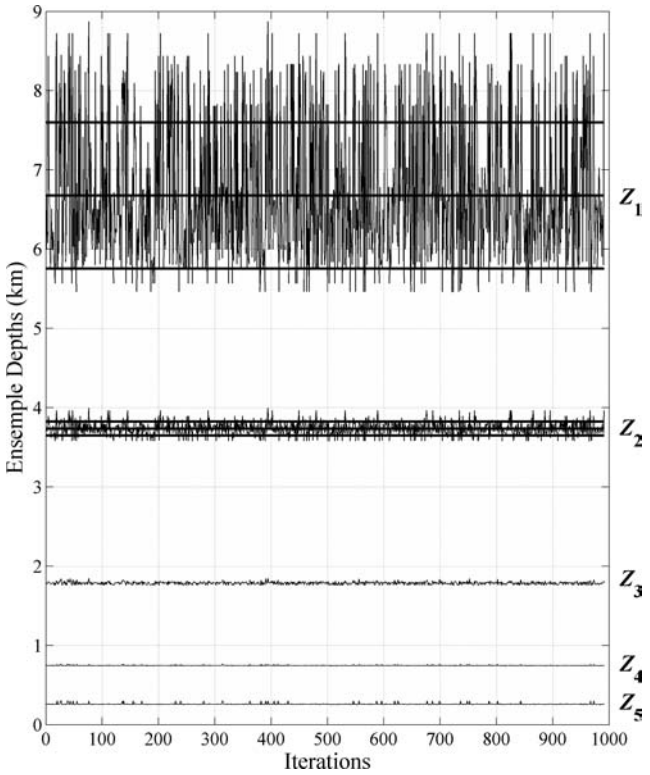

Figure 7. Estimation of the depth to the magnetic source ensembles based on eq. (1) and 1000 random realizations of the radially averaged power spectrum (see the text for details). The horizontal lines indicate the expectation values and 68 per cent confidence limits of the two deeper ensembles (Z_1 and Z_2).

resolution of short wavenumbers so that broader averaging annuli (lower resolutions) would bias the solution to shallower depths and vice versa. Conversely, the depths to the shallower (depth-limited) ensembles are rather consistently determined in both higher and lower resolution power spectral realizations because their localization is less sensitive to the averaging scheme. Because non-linear least-squares solvers are local, it is also easy to ascertain that different starting models (A_j, Z_j, A_n) may easily result in different estimates of the depth to the basal layer even for the same realization of the radial spectrum. However, and as will become abundantly clear in Section 4.3, the determination of trustworthy parameters for the basal layer is very important. In consequence, the problem of finding maximum likelihood estimates of the parameters A_j, Z_j and A_n must be treated statistically. The solution given herein implements a bootstrapping approach as follows: random realizations of the radial spectrum are generated, to which random starting models are assigned and used by the non-linear least-squares solver to find a best-fitting (local) solution. The process is repeated many times over so as to generate large populations of strength estimates $\{\hat{A}_j\}$, depth estimates $\{\hat{Z}_j\}$ and noise estimates $\{\hat{A}_n\}$, each associated with 95 per cent confidence intervals $\{\delta\hat{A}_j\}$, $\{\delta\hat{Z}_j\}$ and $\{\delta\hat{A}_n\}$, respectively. Finally, the expectation values $\langle A_j\rangle$, $\langle Z_j\rangle$ and $\langle A_n\rangle$ are estimated in a least-squares sense as $\langle X_j\rangle = \sum\{\hat{X}_j w_j\}/\sum\{w_j\}$, with $\{w_j\} = \{1/\delta\hat{X}_j\}$. Fig. 7 illustrates depth estimates obtained after 1000 iterations of the procedure; Table 2 presents the final expectation values obtained after 5000 iterations. The depth to the basal layer exhibits the expected variability, nevertheless, the weighted average $\langle Z_1\rangle$ appears to be a fair compromise and leans towards the higher density of $\{Z_1\}$ determinations, implying that estimates greater than 7.5–8 km are generally associated with larger errors. Approximately 72 per cent of $\{Z_1\}$ lies within one standard deviation of the expectation value. This leaves a small population of upward biased (>8 km) determinations to form what appears to be their own distribution. All the other depth populations $\{Z_2\}$ to $\{Z_5\}$ are consistently determined. Analogous results are obtained for the strengths $\{A_j\}$, but are not shown for the sake of brevity.

The final results indicate that the *basal* (depth-unlimited) sources are located at depths greater than approximately 7 km *below flight level* (BFL). In terms of power, the most significant contributions to the magnetic anomaly map appear to be made by large-scale sources buried deeper than 4 km BFL. These will henceforth to be referred to as *deep* structures and will receive particular attention in the ensuing analysis. Smaller contributions are made by an ensemble of *shallow* structures extending between 0.3 and 1.8 km BFL, or 0 and 1.5 km below the surface. These are generally local and as will be seen shortly, they may be attributed to ophiolitic and volcanic formations, either buried or outcropping. Some of the shallow sources also appear to be genetically related to the deep ensemble in the sense that they comprise extensions of deeper structures, as for instance in the vicinity of the MVC. The remaining of this section is devoted to the separation and examination of anomalies generated by the deep and shallow structures using the efficient anomaly separation scheme introduced in the Appendix.

4.3 Separation of anomalies according to source depth

The results of the 'anomaly separation' exercise are shown in Figs 8–11 and have all been obtained with the Radial Extended Meyer Window filter described in the Appendix. Fig. 8 illustrates the large-scale anomalies generated by the *basal* geological sources (depths greater than 6.8–7 km). Two main anomalies of comparable amplitude can be observed: one developing beneath the east coast of the Peloponnese in the west, and one along MVC–Cape Skillaion line (*Skl–MVC* in Fig. 8), exhibiting overall NW-SE elongation. A relatively low-amplitude (approximately 10nT) anomaly elongated in the W-E direction appears to develop beneath Crommyonia and Megaris (*CM* in Fig. 8). The *Skl–MVC–CM* anomalies are aligned on the 100 km contour of the subducting slab. This is consistent with the depths at which low-temperature and high-pressure mineral phase transitions involving the growth of dense anhydrous minerals (garnet and eclogite), drive water out of the slab and into the mantle wedge, thereby initiating flux-melting processes that generate andesitic magmas and arc volcanism (e.g. Grove *et al.* 2006, and references therein). The basal anomalies are truncated, as they extend beyond the boundaries of the aeromagnetic survey. As a result,

Table 2. The strength and depth parameters of magnetic source ensembles, calculated on the basis of 5000 solutions to eq. (1) obtained with the bootstrapping procedure described in the text.

Ensembles	1	2	3	4	5	A_n
$\langle A_j\rangle \pm \sigma_{\langle Aj\rangle}$	63.36 ± 10.9	443.97 ± 43.29	28.03 ± 0.53	0.11 ± 0.03	$2 \times 10^{-4} \pm 1 \times 10^{-5}$	$1.6 \times 10^{-5} \pm 2 \times 10^{-6}$
$\langle Z_j\rangle \pm \sigma_{\langle Zj\rangle}$	6.8 ± 0.92	3.74 ± 0.09	1.8 ± 0.02	0.75 ± 0.004	0.3 ± 0.009	

Notes: Results are given in the form of ensemble averages $\langle X\rangle$ and ensemble standard deviations ($\sigma_{\langle X\rangle}$).

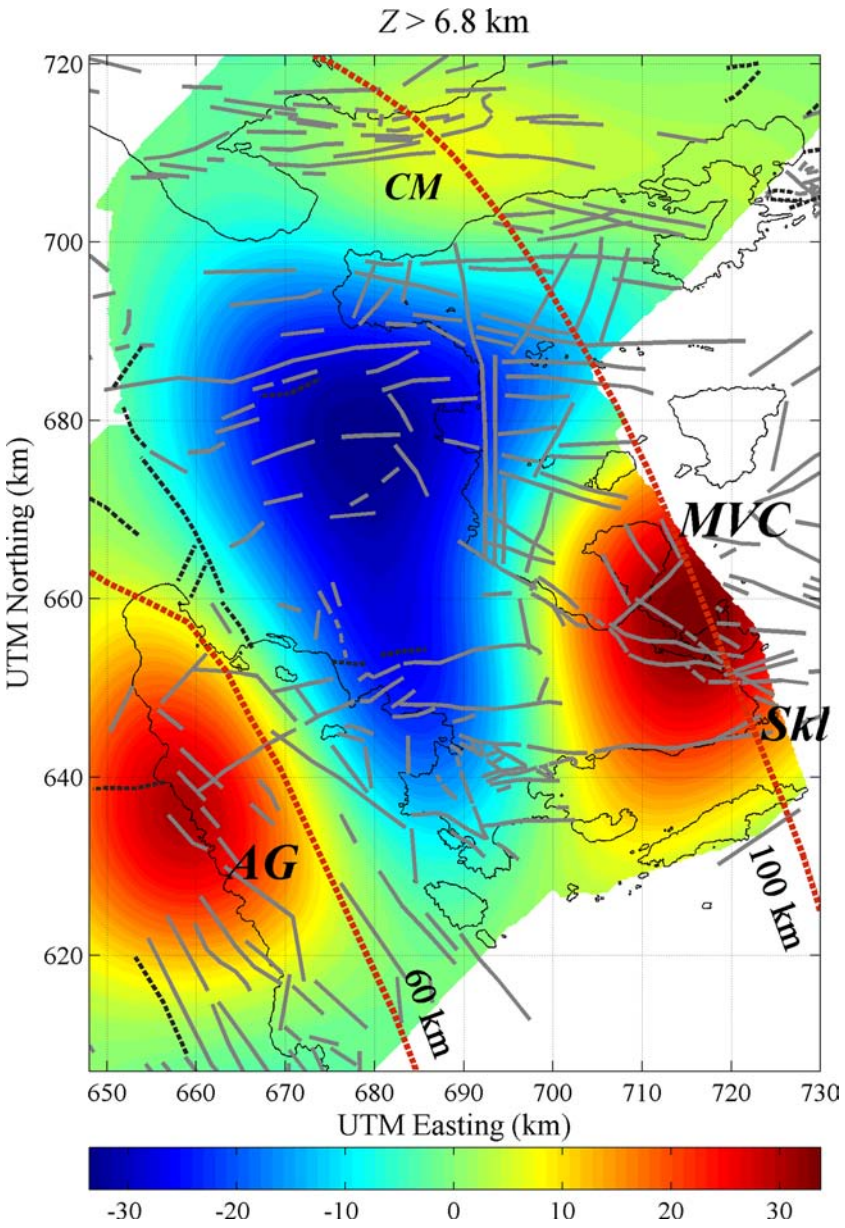

Figure 8. RTP magnetic anomalies generated by basal (depth-unlimited) sources, buried at depths greater than 7 km below flight level (low-pass filtered). Magnetic intensity units are given in nT. The anomalies are geographically referenced: *AG*: Argolic Gulf; *Skl*: Cape Skillaion; *MVC*: Methana Volcanic Complex; *CM*: Crommyonia–Megaris. Broken lines indicate the location of the 60 and 100 km isodepths to the top of the subducting slab (after Basili *et al.* 2013). UTM northings were reduced by 3500 km so as to facilitate the display.

their large-scale geological source formations cannot be effectively constrained; this may be a plausible explanation as to why they appear to be depth-unlimited in the radially averaged power spectrum, although they certainly lose their magnetization at depths 12–14 km (depth to Curie isotherm).

Fig. 9 illustrates the anomalies generated by the deep depth-limited source ensembles and specifically those located at depths between 7 and 4 km BFL. These are generally of lower amplitude (up to 65 nT), but larger scale and appear to be arranged in two distinct orientations:

(1) Approximately N310°–N320° parallel to the east coast of the Peloponnese and along the axis of the Argolic Gulf (marked *AG* in Fig. 9), as well as between Cape Skillaion, MVC and Crommyonia (*Skl–MVC–Dhi* line of Fig. 9). Notably, the former (*AG*) anomalies are roughly aligned with the surface projection of the 60 km isodepth; the significance of this observation will be discussed in Section 5 under the light of additional information. The latter anomalies are roughly but conveniently aligned with the 100 km isodepth of the subducting slab. Attention is also drawn to the Dhiaporian islet anomaly (*Dhi* in Fig. 9), which appears exclusively undersea in the Gulf of Megara and is tightly framed by faulting structures.

(2) Approximately W-E between the areas of Epidavros and MVC (*EDA–MVC* in Fig. 9), as well as along the Argolic Gulf–Hermionis–Hydra Gulf–Cape Skillaion axis (*AG–Her-HdG–Skl* in Fig. 9).

Fig. 10 illustrates *intermediate* anomalies generated by sources buried between 4 and 2 km BFL. These are significantly more

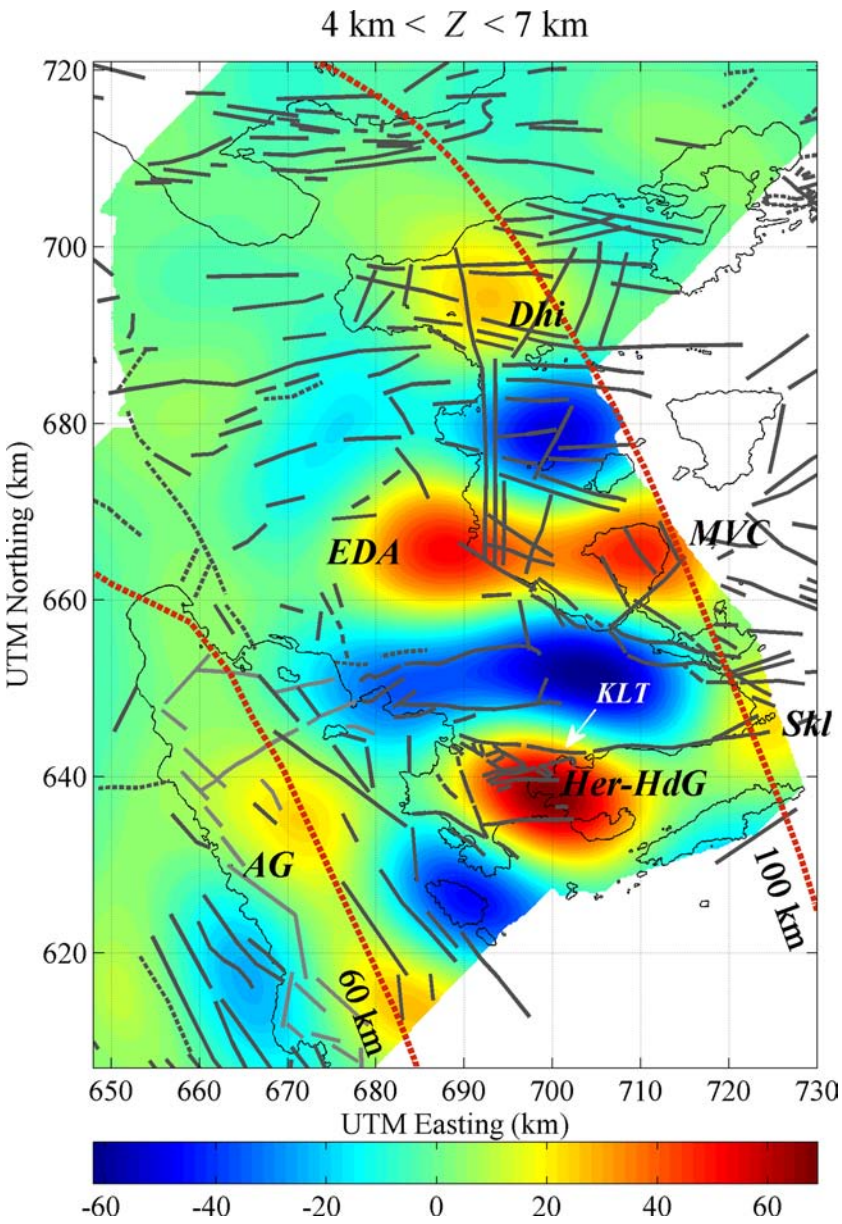

Figure 9. RTP magnetic anomalies generated by sources buried at depths between 7 and 4 km below flight level (bandpass filtered). Magnetic intensity units are given in nT. The geographic references are: *AG*: Argolic Gulf; *Her-HdG*: Hermionis-Hydra Gulf anomaly; *Skl*: Cape Skillaion anomaly; *MVC*: Methana Volcanic Complex; *EDA*: Epidavros Deep Anomaly; *Dhi*: Dhiaporian Islets–Megara Gulf anomaly. *KLT* is the Koilada-Loutra-Thermisia fault zone. Broken lines indicate the location of the 60 and 100 km isodepths to the top of the subducting slab (after Basili *et al.* 2013). UTM northings were reduced by 3500 km so as to facilitate the display.

localized and of slightly larger amplitude in comparison to the deep-source anomalies (up to 100 nT), except in the area of the MVC where amplitudes rise to approximately 200nT. Specifically, one may observe:

(1) Alignments of N310°–N320° orientation along the axis of the Argolic Gulf (*AG*), collocated with the trace of the 60 km isodepth of the subducting slab, as well as along the axis Cape Skillaion (*Skl*)–Poros Island (*Por*)–*MVC*–*Dhi* Islets and *CM*, collocated with the 100 km isodepth of the subducting slab (see above). A rather low-amplitude (up to 30nT) alignment of localized anomalies with similar orientation develops to the NW of Hermionis, along the east coast of the Argolic Gulf between coordinates (E641, N680) and (E667, N670); it is indicated with a series of question marks.

(2) Alignments of approximately W-E orientation along an axis through the Argolic Gulf (*AG*), *Her*, Hydra Strait (*HdS*) and Cape Sklillaion (*Skl*), as well as between *EDA* and *MVC*. The latter is apparently associated with the deep *EDA*–*MVC* anomaly, which would appear to split into two localized features (*EDA* and *MVC*) at intermediate depths. A rather significant anomaly of approximately 140nT at peak is observed at the area of Radon (*Rd*). This appears isolated although there is strong indication that it may be connected to the Poros Island anomaly (*Por*) via a low-amplitude anomaly of approximately 15nT through the area of Kalloni (*Kl*). Finally, an alignment of localized sources with relatively low amplitudes (up to 60nT) and roughly W-E orientation appears at approximately 680N and 670E–710E, apparently bracketed by two lineaments of similarly oriented faults.

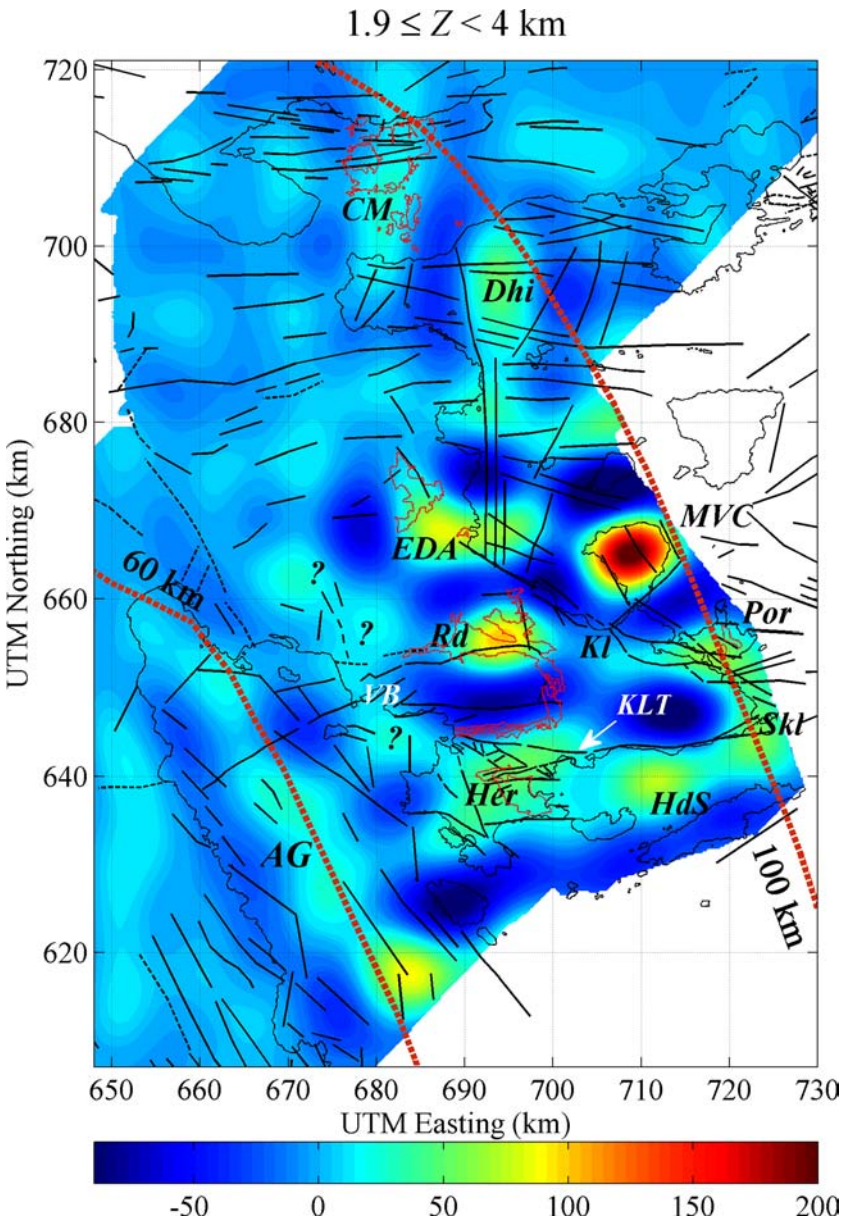

Figure 10. RTP magnetic anomalies generated by sources buried at depths between 2 and 4 km below flight level. Magnetic intensity units are given in nT. The geographic references are: *AG*: Argolic Gulf; *Her*: Hermionis anomaly; *HdS*: Hydra Strait anomaly; *Skl*: Cape Skillaion anomaly; *Por*: Poros anomaly; *MVC*: Methana Volcanic Complex; *EDA*: Epidavros Deep anomaly; *Rd*: Radon anomaly; *Kl*: Kalloni; *Dhi*: Dhiaporian Islets–Megara Gulf anomaly; *CM*: Crommyonian anomaly. *VB* marks the location of Vourlos Bay and *KLT* is the Koilada-Loutra-Thermisia fault zone. Broken lines indicate the location of the 60 and 100 km isodepths to the top of the subducting slab (after Basili *et al*. 2013). UTM northings were reduced by 3500 km so as to facilitate the display.

The *Dhi* anomaly can also be observed at intermediate depths with a maximum amplitude of 60–70 nT. It is again tightly framed by faults but is now stretched in an N-S direction, apparently in response to the corresponding stretching of the causative body and presumably in association with the N-S component of the framing fault system. A localized, N-S oriented anomaly of similar amplitude also appears at the area of Crommyonia (*CM*). Signatures of intermediate sources that are *not* observed at depths greater than 4 km appear at *Kl*, *Rd*, along the east coast of the Argolic Gulf (marked as '*?*') and *CM*. Some of these may be due to recent igneous intrusions. Some intermediate anomalies appear at areas adjacent to, or coinciding with Mesozoic ophiolitic outcrops; examples of the former can be seen at *EDA* and *Her*, while characteristic example of the latter is *Rd*. These anomalies will be discussed in Section 5, after additional information is presented. As a general rule, however, the deep and intermediate sources (2 km $< Z <$ 7 km) are arranged in distinctive W-E and NW-SE (N310°–N320°) configurations, are generally massive and are spatially correlated with extensional tectonic structures and the HVA as in the case of the *Skl–Por–MVC–Dhi–CM* alignment. This clearly distinguishes them from the shallow-buried ($Z <$ 2 km) sources which are generally distributed and of local scale, as will be shown forthwith.

The final Fig. 11 illustrates magnetic anomalies, associated with shallow (but not superficial) sources (0.3 km $< Z <$ 1.8 km). These are generated by a complex of distributed near-surface formations consisting of buried or extrusive volcanics and outcropping or shallow-buried ophiolites. The highest amplitudes (100–720 nT) are observed in association with the extrusive volcanics of Methana

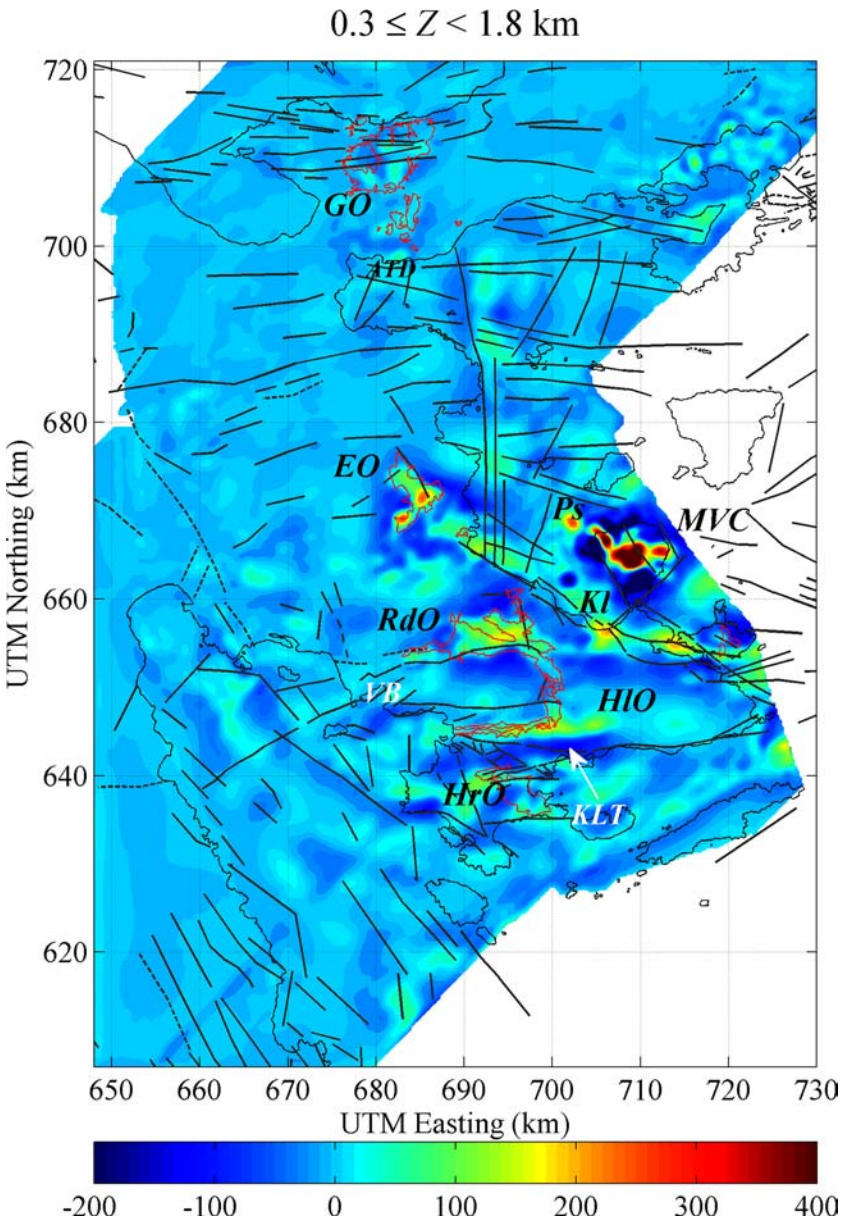

Figure 11. RTP magnetic anomalies generated by sources buried between 2 and 0.3 km below flight level. Magnetic intensity units are given in nT. The geographic references are: *HlO*: Heliokastron Ophiolites; *HrO*: Hermioni Ophiolites; *RdO*: Radon Ophiolites; *Kl*: Kalloni anomaly; *MVC*: Methana Volcanic Complex; *Ps*: Pausanias submarine volcano; *EO*: Epidavros Ophiolites; *ATD*: Aghioi Theodoroi Dacite; *GO*: Gerania Ophiolites. *VB* marks the location of Vourlos Bay and *KLT* is the Koilada-Loutra-Thermisia fault zone. The outcrops of *HlO*, *HrO*, *RdO*, *EO* and *GO* are also outlined in red. UTM northings were reduced by 3500 km so as to facilitate the display.

peninsula, while the ophiolites, on account of being generally altered and weathered, are associated with appreciably lower amplitude anomalies (20–150nT in general and up to 240nT at Epidavros).

The distinctive NW-SE and W-E configuration of the deep and intermediate sources cannot be observed at their respective locations and is replaced by a pattern of distributed, local, low-amplitude anomalies, as for instance along the Argolic Gulf and along the Hermionis peninsula–Hydra Gulf–Cape Skillaion line. In many cases, such anomalies could be attributable to intrusive activity, particularly in the neighbourhood of the MVC. The high-amplitude Methana anomalies are principally associated with the central domes of the volcanic edifice (up to 700 nT), the distinctive lava flow of the 230 BCE eruption at the immediate NW of the central domes (approximately 725nT) and the Pausanias submarine volcano (*Ps* in Fig. 11), right to the NW of the peninsula. Additional, anomalies related to the MVC include the areas of *Kl* and the Poros-Troezenia strait where the anomaly is directly associated with a small andesitic outcrop (Poros andesite). Three small-scale anomalies appear at the location of the deep *Dhi* Islets anomaly; these may be offshoots a deeper seated pluton. The localized low-amplitude (<40 nT) anomaly marked *ATD* is the signature of the small dacitic outcrop found at the Aghioi Theodoroi area of Crommyonia. Moreover, the area of the Sousaki solfatara does not appear to generate any significant magnetic signature.

Ophiolite outcrops generate distinctive magnetic signatures. The Epidavros ophiolites (*EO*) produce a significant anomaly that is clearly delimited by the outcrop, while the Gerania (*GO*) and

other Crommyonian ophiolites exhibit a patchwork of rather low-amplitude anomalies (<70 nT), also completely delimited by the outcrops. Conversely, the Fournoi–Heliokastron anomaly (*HlO*) extends to the east of the outcrop, its source presumably buried under the Pelagonian flysch. A low-amplitude anomaly (<100 nT) also develops around the small outcrop of Nea Epidavros, to the SE of *EO* and the Radon outcrop (*RdO*) is also collocated with a 150 nT anomaly which extends beyond the boundaries of the outcrop. The anomalies associated with the Hermioni ophiolites (*HrO*) are clearly insignificant. It is also worth noting that the outcrops of South Argolid ophiolites (*RdO* and *HlO*) are characteristically elongated in the W-E direction and correlated with local W-E tectonic lineaments. We shall argue in Section 5, that is a result of tectonic activity, possibly the same as the one that modulated the configuration of the deep sources.

5 DISCUSSION AND CONCLUSIONS

Herein, we examine aeromagnetic data collected over a broad area of Northeast Peloponnesus (Argolid, eastern Corinthia and the Argolic and Saronic gulfs), for evidence of deep and shallow calc-alkaline syn-rift magmatism related to the broader CR system and the HVA. The analysis is semi-quantitative: in a first step, we identify ensembles of magnetized geological bodies (magnetic field sources) buried at different depths with parametric modelling of the radially averaged power spectrum; in a second step, we use a bank of efficient, automatically scalable wavelet filters to separate the anomalies associated with these ensembles and evaluate their configuration, extent, nature and contribution to the composition of the total (aero)magnetic intensity map of the study area. A cardinal part of our work is to evaluate the relationship between the different magnetic source ensembles and the active tectonics of the study area, as a means of inferring their nature, origin and current disposition. To this effect, we also evaluate the contemporary stress field—hence the expected faulting pattern—with formal inversion of all known and well-constrained earthquake focal mechanisms and interpret the existing neotectonic ken under the light of our findings.

5.1 Contemporary crustal deformation

According to the analysis of Section 3, the expected principal direction of normal faulting modes in the study area is WNW-ESE (N290°), which is mainly observed along the northern coast of Argolis peninsula and in the Saronic Gulf, and NW-SE (N130°) mainly observed in offshore faults along the northern margin of the Argolic Gulf, between Spetsai Island and the head of the Gulf. An interesting outcome of the same analysis is the recognition of local-scale W-E and NW-SE (N330°) oriented faulting, respectively, consistent with the synthetic (dextral) R-shear and antithetic (sinistral) R´-shear directions of Riedel's shear theory. The latter may comprise a significant component of local crustal deformation, as we discuss below.

W-E faults have been mapped by various authors both onshore and offshore in the Argolic and Saronic gulfs; a very interesting such feature is the well-defined offshore alignment of epicentres between Aegina and Salamis islands detected by Drakatos *et al.* (2005), which has been interpreted to comprise a southerly extension of the GoC normal fault system. According to our results, the W-E faulting direction is consistent with the synthetic (dextral) R-shear direction. In this respect, it is plausible that at least in the area south of 38.7°N, the W-E faults are more than just southerly expressions of the GoC normal faults. Rather, they may comprise structures inherited from the inception of the CR (hence related to the GoC system), but which have evolved to accommodate the strain differential caused by the apparent disparity of extensional trends in the Argolic and Saronic gulfs by developing non-trivial right-lateral heave. It is also conceivable that the W-E faults are oblique-normal (of transtensional nature), as can be observed in a few focal mechanisms of the southern Argolid and the Argolic Gulf (Table 1 and Fig. 3). The origin of the different extensional trends in the Argolic and Saronic gulfs is yet to be specified and we note that this problem will be revisited in follow-up work and will be addressed with additional observational data.

Faults of NW-SE (approximately N330°) orientation, parallel to the antithetic (sinistral) R´-shear direction have rarely been mapped in the Argolid with the possible exception of onshore and offshore features observed in the vicinity of the MVC (also see Papanikolaou *et al.* 1988). Note, however, that this orientation is almost parallel to the strike of the Argolic Gulf and Plain, the east coast of Peloponnesus and the faulting structures observed therein (SW quadrant of Fig. 3). It is also parallel to the local trend of the HVA and the subducting slab (e.g. Fig. 1; also see Suckale *et al.* 2009, and references therein). Accordingly, it should not be dismissed as it may represent some kind of coupling between the rapidly southwesterly moving Aegean continental forearc and the slowly northeasterly subducting slab.

5.2 Deep magnetic anomaly sources: origin and relationship to regional tectonics and the Hellenic subduction

The analysis presented in Section 4 indicates that magnetic field sources buried at depths greater than 2 km are clearly distinguishable from those buried at shallower depths. The former comprise generally elongate and massive formations arranged in a distinctive W-E and NW-SE (N310°–N320°) configuration; these are spatially correlated or bracketed by the major extensional or transtensional neotectonic structures, or are directly located on the HVA (along the axis *Skl–Por–MVC–Dhi–CM* of Figs 8 and 9, which includes two known volcanic fields). Given that the ophiolites generally comprise dismembered thin nappes of tectonic mélange emplaced by thin-skinned overthrusting and are thus unlikely to generate significant deep-seated magnetic anomalies, it is plausible that the deep and intermediate sources are actually magmatic intrusions (dioritic–granodioritic plutons) whose placement is, or has been controlled by *syn-rift* tectonic activity. Intermediate depth ($2\,\mathrm{km} < Z < 4\,\mathrm{km}$) sources are generally more localized than the deep sources ($4\,\mathrm{km} < Z$), but this is not difficult to explain: if they are of igneous origin, then the intermediate sources should be localized extensions of the deep sources formed by ballooning, wedging or branching of the main plutons toward the surface. Sources buried at depths shallower than 2 km are generally local and distributed, in most cases directly identifiable with ophiolitic outcrops and extrusive calc-alkaline volcanics (also see below). There are, however, some 'grey areas' in the depth interval 2–3 km, where the extensions of the deep (plutonic) sources may overlap or even merge with the deeper roots of shallow sources. We shall now proceed to justify our interpretation and discuss the nature and disposition of the magnetic field sources, with particular reference to the deeper ensembles.

The surface of the study area features two types of geological formations capable of generating significant magnetic anomalies: ophiolitic mélange and calc-alkaline extrusive rocks (andesites to

dacites) associated with the MVC. As found by Efstathiou (2011), the magnetic susceptibility of the ophiolitic formations averages to 11×10^{-3} with a median of 2×10^{-3} and range of 0.02×10^{-3}–36×10^{-3}. Respectively, the susceptibility of the extrusive volcanics averages to 20×10^{-3} with a median of 17×10^{-3} and a range of 5×10^{-3}–26×10^{-3}. The ophiolitic mélange has formed in accretionary prisms and obducted onto its present position by gravity sliding (olistostromes), or by thin-skinned overthrusting. The Gerania (Crommyonian) ophiolite outcrop is associated with low-amplitude (<80 nT) anomalies, as one would expect of a rather thin nappe consisting of serpentinized harzburgites, with magnetic susceptibilities no higher than 15×10^{-3}: it can safely be concluded that the thickness of the Crommyonian ophiolites is significantly smaller than 1 km, so that any anomaly generated by sources under this depth could be attributed to igneous (dacitic) intrusions. The mélange of the north and central Argolid consists of radiolarites intercalated with 10–30 m thick ophiolitic olistostromes comprising agglomerates of medium-sized ophiolitic olistolites and having undergone static greenschist metamorphism. Chaotic deposition, metamorphism and chemical alteration associated with the depositional environment generally diminish or even completely destroy magnetic susceptibility, as confirmed by the measurements. The mélange of the southern Argolid consists of a schistose serpentinitic matrix with medium- to large-size ophiolitic blocks and apparent thicknesses of up to 200 m (Gaitanakis & Photiades 1991, 1993). This unit is also characterized by suprasubduction-related geochemical signature as well as extensive alteration and static greenschist metamorphism, all of which account for the low magnetic susceptibilities measured by Efstathiou (2011), even in the healthier (least weathered) rock samples. Several magnetic anomalies generated by sources shallower than 2 km can be directly identified with ophiolitic formations in the Argolid (Fig. 10). These are the *EO* (with amplitude up to 300 nT), the Radon Ophiolites (*RdO*, up to 240 nT), the *HlO* (up to 150 nT) and the *HrO* (up to 130 nT). These amplitudes can be safely attributed to the physical characteristics (apparent thicknesses and susceptibilities) of the ophiolitic mélange, as determined by surface observations. As can be easily demonstrated by analytic continuation and without factoring in the demagnetizing effect of the geothermal gradient, if the respective ophiolitic formations were buried at depths of 2.5 or 4 km, they would generate anomalies no higher than 40 and 16 nT which are at least 50 per cent lower than the lowest amplitude attributed to intermediate and deep sources (Figs 8 and 9). Conversely, if deeply buried ophiolitic formations were to account for the observed deep-source anomalies, they would either have to be forbiddingly massive with respect to their observed physical characteristics and emplacement process, or they would have to have much higher susceptibility (i.e. different composition).

In continuing our discussion of the sources of magnetic anomalies in the study area, we note that well-informed researchers (e.g. Piper, 2016, personal communication) have contemplated the possibility of magnetic anomalies being—partially at least—generated by Triassic lavas (represented by thin pyroclastics at Epidavros), or Hercynian plutons in the Pelagonian basement (e.g. as summarized in chapter 2 of Pe-Piper & Piper 2002). The former rock formation has been described by Gaitanakis & Photiades (1991) as consisting of olistolites of lavas and radiolarites with diameters generally smaller than 30 cm, embedded in turbiditic volcano-sedimentary formations with apparent thicknesses of 40 m on average. The nature of these formations suggests that as with the ophiolites, their igneous material should have undergone extensive processing and alteration and should be largely demagnetized. In support of this assessment, we note that eastward of Vourlos bay (*VB* in Figs 10 and 11), where such formations have been observed to outcrop, there are no magnetic anomalies at depths greater than 2 km (Fig. 10) and very weak anomalies, of the order of a few nT, at depths shallower than 1.8 km (Fig. 11).

Massive granitoid plutons in the Pelagonian basement are observed in the western and central Macedonia, Greece; these are dated to the Upper Carboniferous and are unconformably overlain by terrigenous metasediments of probable Permian to Middle Triassic age (e.g. Kotopouli *et al.* 2000; Pe-Piper & Piper 2002). As can be easily verified by overlaying the geological (Kotopouli *et al.* 2000) and aeromagnetic (Chailas *et al.* 2010) maps of W. Macedonia, these formations are either completely non-magnetic as in the Pieria, Deskati and Olympiada complexes, or exhibit localized anomalies as in the case of the Varnountas pluton. Such massive basement plutons are not observed in the rest of the Pelagonian zone and their presence in the Argolid has never been established. Gaitanakis & Photiades (1991) have observed three small granodiorite outcrops with sizes not exceeding 50×10 m along the strike of the Koilada-Loutra-Thermisia fault zone (*KLT* in Figs 9–11), which they interpret to comprise fragments of the local Pelagonian crystalline basement. These, however, have been dated to the Mid-Late Jurassic on the basis of U–Pb igneous zircon dating (Photiades & Keay 2000). Moreover, the geological field data provide no indication whatsoever as to the existence of sizeable granodioritic bodies beneath the outcrops (or beneath the entire Argolid for that matter). At depths between 7 and 2 km, the *KLT* fault zone appears to form the northern boundary of the *Her-HdG* (Fig. 9), *Her* and *HdS* (Fig. 10) group of anomalies. Although one might suggest that these anomalies have been generated by 'massive' basement plutons, we can argue that this is certainly not the case. Along the *KLT* fault zone and at depths shallower than 2 km there is absolutely no indication of shallow-buried magnetized rock formations and any anomaly observed to the north of the zone can be directly and exclusively attributed to the *HlO* ophiolitic suite (Fig. 11). This means that the granodiorite outcrops observed along *KLT* are either non-magnetic, or are very small and localized, lacking continuity and deeper roots. There are no studies of a possible relationship of the Argolid granodiorite basement outcrops with the massive Carboniferous Pelagonian plutons of western Macedonia and, given their vastly different sizes and ages, their correspondence cannot be asserted. Given also the largely non-magnetic nature of the Macedonian plutons and the apparently non-magnetic nature of the Argolid Pelagonian basement's granodiorites, the plausibility of aeromagnetic anomalies generated by 'massive' magnetized 'ancient basement plutons' at depth cannot be entertained.

The magmatic nature and origin of the N310°–N320° and W-E oriented deep-source anomalies is all the more plausible because they are collocated with the axes of contemporary extensional (N310°–N320°) or trans-tensional (W-E) neotectonic structures and the N310°–N320° oriented HVA: let alone that rifting processes favour intrusive magmatism, it is rather difficult to dispute the magmatic origin of deep sources in the vicinity and along the HVA, as well as around the MVC. The relatively elevated heat flow of southern Argolid, (50–70 mW m^{-2} according to Taktikos 2001), is consistent with this idea. The concept of recent plutonic activity could be strengthened by comparison with analogous Miocene plutonism in the Cyclades. As Piper (2016, personal communication) pointed out, this plutonism is in many places localized along major strike-slip faults, but with lighter granitic magmas ballooning out along mid-crustal extensional detachment surfaces. Mafic magmas are more abundant at deeper crustal levels (e.g. Delos).

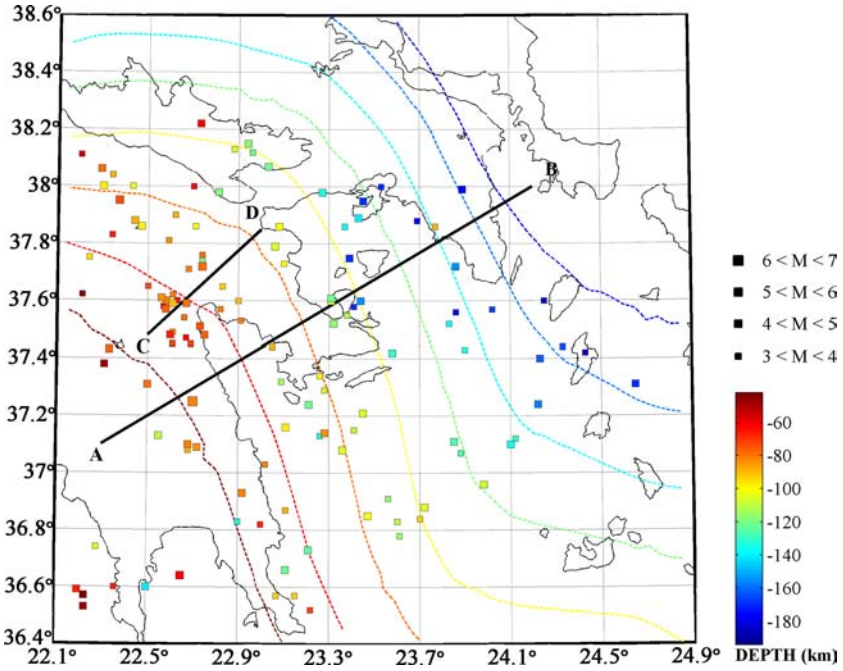

Figure 12. The hypocentral distribution of subcrustal (>40 km) earthquakes observed in the broader study area over the period 1965–2012. Earthquake data have been extracted from the online bulletin of the International Seismological Centre (http://www.isc.ac.uk). Only earthquakes with $m_b \geq 3.5$ mag are shown. AB marks the geographical location of the cross-section shown in Fig. 13 T. CD marks the location of the magnetotelluric cross-section shown in Fig. 13. The broken lines represent are isodepths of the ceiling of the subducting slab and have been extracted from the SHARE database (Basili *et al.* 2013).

The crystallization depth of the strike-slip-related western granodiorite pluton of Naxos is fairly well constrained by mineralogy of the thermal aureole and geobarometry of hornblende to 1.5–2.5 kbar or 5–8 km (Pe-Piper 2000), similar to the depths of the magnetic sources detected herein. Mafic enclaves are very abundant in some volcanic rocks on Methana (Pe-Piper & Piper 2013) and are known at Crommyonia/Sousaki (where some of the oldest rocks are andesitic).

As mentioned above, it is rather difficult to contend the magmatic origin of deep magnetic field sources in the vicinity of the HVA. Conversely, it is necessary to illustrate the plausibility of the magmatic nature of deep sources along the axis of the Argolic Gulf and Plain. Fig. 12 shows the epicentral distribution of subcrustal (>40 km) earthquakes observed over the broader study area and over the period 1965–2012. The data have been extracted from the online bulletin of the International Seismological Centre (http://www.isc.ac.uk); only earthquakes with magnitudes $m_b \geq 3.5$ are shown and plotted on their primary ISC location coordinates. The ISC catalogue was favoured because it is based on a large, trans-border observational data set and advanced hypocentre location techniques (Bondar & Storchak 2011) that have also been used to relocate earthquakes since 1965. In comparison to the other definitive earthquake catalogues of the broader study area, the ISC bulletin provides the more complete and consistent source of deep seismicity information since 1965. Fig. 13 is a composite SW-NE section across our study area. The bottom panel of Fig. 13 illustrates: (i) the projection of the subcrustal earthquake hypocentres of Fig. 12 on the profile AB of Fig. 12. (ii) The electrical resistivity cross-section along the profile CD of Fig. 12, rotated parallel to AB and projected on the AB plane; this information was extracted from the deep magnetotelluric profile of Galanopoulos *et al.* (2005) and was generously provided by Dr V. Sakkas and Dr E. Lagios of the University of Athens (personal communication). (iii) A profile of the Mohorovičić discontinuity of the Aegean plate according to Sachpazi *et al.* (2007), collocated with profile AB. (iv) A profile of the Mohorovičić discontinuity of the Aegean plate according to Suckale *et al.* (2009), rotated to the orientation of AB and projected on the AB plane. (v) A profile of the ceiling of the subducting slab taken from the tomographic image of Fig. 1 of Sachpazi *et al.* (2016), which is approximately collocated with the CD plane; this has been rotated to the orientation of AB and projected on the AB plane. The top panel of Fig. 13 is a vertically exaggerated topographic section along AB, together with major normal faults (as per Fig. 2).

The location of the subducting slab is clearly defined by the distribution of earthquake hypocentres. The light grey line envelops and approximately outlines the slab; it is a means of visualization enhancement and does not represent its true thickness. The slab dips eastwards at an *apparent* angle of 20° up to the Argolic Gulf and 40°–45° thereafter. An inflection appears exactly below the Argolic Gulf, at a depth of approximately 65 km, consistently with Hatzfeld *et al.* (1989). Inflection has also been imaged at the *same* depth by the tomographic study of Sachpazi *et al.* (2016), along the CD plane. The size of an apparent dip angle depends on the orientation of the section along which it is measured. Simple calculations show that for the shallow dipping leg of the slab, the discrepancy is very small between the earthquake and tomographic data. For the steep-dipping leg however, it may account for up to 4° (~40 per cent) of the difference observed in the plunges of the two profiles, the remaining being attributable to technical issues (methods of analysis) and the true geometry of the slab relative to the location of the two profiles. Section AB crosses the MVC and as can be readily observed the slab is located at approximately 110 km beneath the volcano. This is consistent with the depth at which low-temperature and high-pressure mineral phase transitions involving the growth of dense anhydrous minerals (garnet and eclogite), drive aqueous fluids into the mantle wedge and initiate the generation of calc-alkaline magmas (e.g. Grove *et al.* 2006, and references therein).

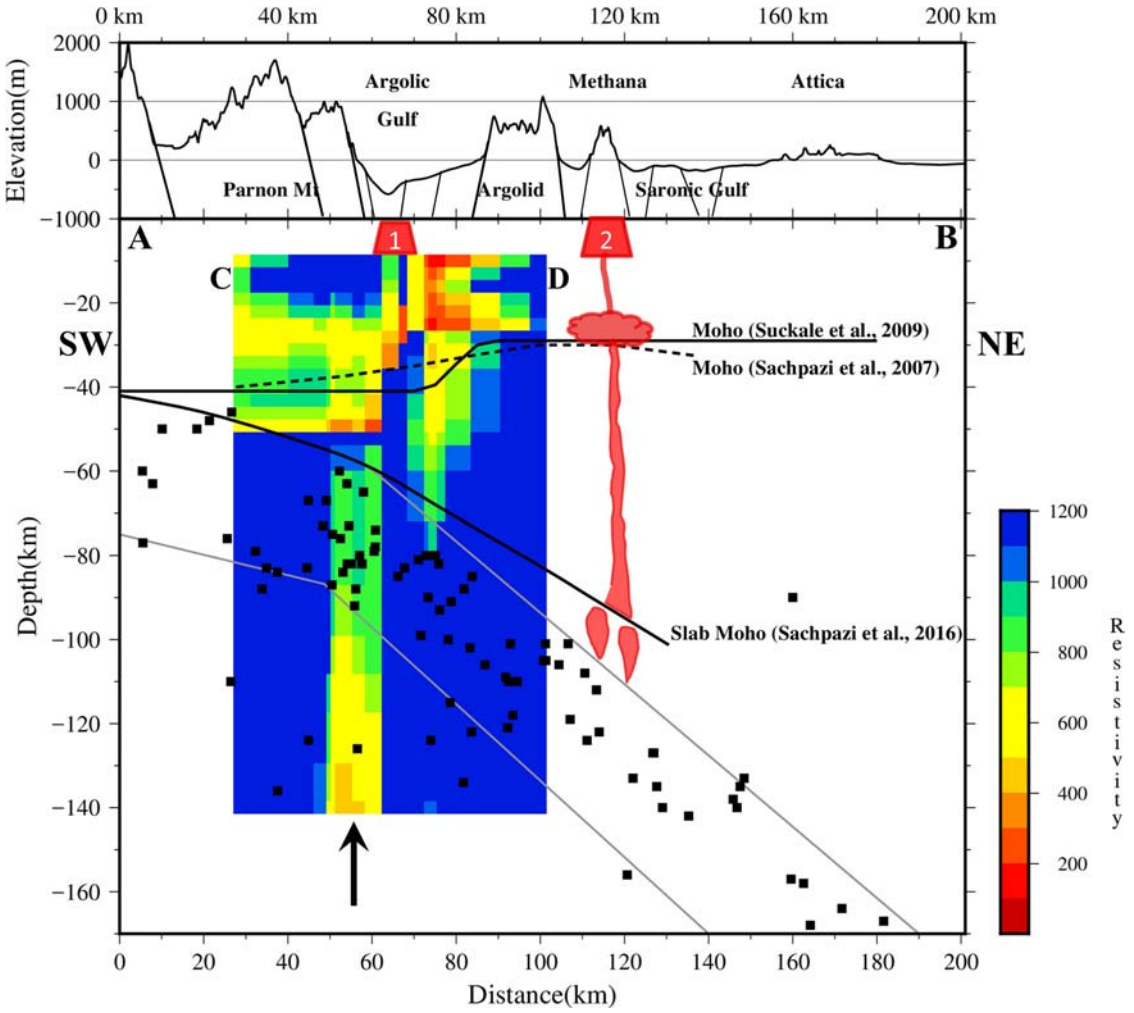

Figure 13. Composite cross-section along the profile AB of Fig. 12. The bottom panel illustrates: (i) the projection of the subcrustal earthquake hypocentres of Fig. 12 on the profile AB. (ii) The electrical resistivity cross-section along the profile CD of Fig. 12, rotated parallel to AB plane and projected on the AB plane. (iii) A profile of the Mohorovičić discontinuity of the Aegean plate according to Sachpazi *et al.* (2007), collocated with profile AB. (iv) A profile of the Mohorovičić discontinuity of the Aegean plate according to Suckale *et al.* (2009), rotated to the orientation of AB and projected on the AB plane. (v) A profile of the ceiling of the subducting slab taken from the tomographic image shown in fig. 1 of Sachpazi *et al.* (2016), which is approximately collocated with the CD plane, rotated to the orientation of AB and projected on the AB plane. The top panel is a vertically exaggerated topographic section along AB, drawn together with major normal faults. The red trapezoids indicate the large magnetic sources detected along the axis of the Argolic Gulf (1) and at the Methana Volcanic Complex (2).

In Fig. 12, it is straightforward to observe a concentration of earthquake activity at the head of the Argolic Gulf, as well as a rough N330° alignment of hypocentres between the head of the Argolic and the GoC. These features are pointed to by an uparrow in Fig. 13 and roughly coincide with the inflection of the slab. It is also straightforward to observe 6 or 7 hypocentres at depths of approximately 120 km beneath the Argolic Gulf and Plain. It is very plausible that these correspond to mislocated events. Note, though, that there are only eight 'outlying' hypocentres in Fig. 13 and of those, six are observed at the same area and depth. It stands to reason that this may not be a mere coincidence, given also the column of reduced resistivity observed at depths between 140 and 60 km just under and within the inflection of the slab (see below).

Very important observations can be made with respect to the electrical resistivity structure (Fig. 13). Within the slab, the inflection is associated with resistivity of the order of 700–900 Ω·m embedded in a domain with resistivity higher than 1100 Ω·m. The occurrence of earthquakes in this range of depths (60–80 km) implies dehydration embrittlement of the subducting metabasite crust: therefore, the drop in resistivity may, partially at least, be attributed to the presence of aqueous fluids and/or partial melting in the slab. This process may also drive water into the mantle wedge and be responsible for the relatively low resistivity observed in the lower crust of the overriding (Aegean) plate, directly above the inflection. It also stands to reason that if the 'outlying' earthquakes beneath the inflection are not mislocated, their association with relatively low resistivity may imply that this region is associated with deep rooted and by all probability significant geodynamic processes. Although this is a very interesting problem, it shall not be pursued herein as it transcends the scope of this work.

Another important observation is the domain of relatively low resistivity (100–500 Ω·m) observed in the mantle wedge and the lower crust of the Aegean plate, immediately above the slab and to the east of the inflection. Significantly enough, this is clearly collocated with the thinning of the Aegean plate beneath the Argolic Gulf and Plain, which can be attributed to tectonics (extension)

as well as sublithospheric erosion due to magmatic underplating beneath the area of the volcanic arc. At any rate, the thinning extends at least between 37°N and 38.4°N and commences right beneath the east coast of the Peloponnesus/west flank of the Argolic Plain, far from the volcanic arc (see fig. 5 of Sachpazi *et al.* 2007); its coincidence with these large-scale extensional structures indicates that tectonics should be the primary genitor. Beneath this region, the slab is located at depths of the order of 60–80 km and has entered the blueschist (amphibolitic) metamorphic facies by which aqueous fluids are driven into the mantle wedge due to chlorite dehydration; this process is thought to cause significant reduction of resistivity (e.g. Manthilake *et al.* 2016, and references therein). Accordingly, we consider plausible that mantle wedge hydration, combined with decompression due to the extensional thinning of the Aegean plate generate magma in the mantle wedge that not only depresses the resistivity, but also ascends to the Aegean crust along the active extensional and trans-tensional fault network, eventually solidifying in the upper crust and generating the deep magnetic anomaly sources (plutons) detected herein.

A final noteworthy observation is that the range of resistivities shown in Fig. 13 for the lower Aegean crust, are compatible with analogous results of magnetotelluric modelling by Pham *et al.* (2000), who have estimated an average of 400 Ω·m beneath the area 22.1°E–22.2°E and 38.0°N–38.1°N. What these authors did not have incentive to observe at that time, is that their study area is almost directly located on the (imaginary) northwestward extension of the Argolic Gulf; they also could not have known that it is located directly above the thinning of the Aegean plate crust, as this was mapped by Sachpazi *et al.* (2007). This implies that the lower crustal resistivity estimated by Pham *et al.* (2000) is likely to have been generated by processes similar to those operating beneath the Argolic Gulf and Plain. If true, this would imply that for the most part, the depression of lower crustal resistivity beneath the entire northeastern Peloponnesus is thermally induced. In turn, this would be consistent with a mechanically weak lower Aegean crust, as demanded by influential models of the inception and evolution of the CR (e.g. Armijo *et al.* 1996; Westaway 2002).

5.3 Intermediate and shallow magnetic anomaly sources

The origin of anomalies generated at depths shallower than 3 km is occasionally not straightforward to assess. This lies with the fact that in some cases intrusion may take place in areas adjacent to ophiolitic masses, or even through them. Two of these cases are the *EA* which is partially fused with the *EO* anomaly and the *Rd*, which is fused with the *RdO* anomaly. In the former case, the source is deeply rooted and evidently offset to the south with respect to the EO outcrop (compare Figs 9 and 10). Given the characteristics of north Argolid ophiolites and by analogy to the *Her-HdG–HdS* deep-source anomaly, the *EA* is more likely to be generated by a pluton. The upper parts of the intrusion may have risen to depths comparable to the deeper roots of the ophiolites (*ca.* 2 km), or even shallower penetrating right through them. In any case, there is no direct evidence of an intrusion through the ophiolitic formation in the area of Epidavros and the separation of anomalies generated by intrusive and ophiolitic sources would not be possible without additional structural information. It can easily be ascertained that the Radon anomaly first appears at a depth of approximately 3 km, where ophiolites are unlikely to exist, and has an amplitude of 20 nT. The main part of the anomaly is generated by sources buried between 3 and 2 km (amplitude up to 160 nT in Fig. 10). Moreover, the anomaly is located on a W-E trans-tensional faulting structure terminating at the strait between Troezenia and Poros Island (Fig. 11 and Section 5.4). Thus, one cannot rule out that the deeper part of the *Rd* is igneous of origin. Nevertheless, the near coincidence of the anomaly and the ophiolitic outcrop does not allow conclusions to be drawn with confidence. In a last comment, it should be noted that the Pausanias submarine volcano (*Ps* in Fig. 11) appears to be a rather minor feature, as its magnetic signature is certainly localized with a source depth apparently less than 2 km.

Turning, finally, our attention to the shallow (<2 km) sources and with particular reference to the southern Argolid, we note that the W-E configuration of the (outcropping or buried) ophiolitic sources may also be explained in terms of tectonics. Faulting processes rupture magnetized rock formations, 'shearing' the local total intensity field and producing lateral gradients. Moreover, they initiate secondary processes that destroy magnetic susceptibility and remanent magnetization by facilitating water infiltration and chemical alteration, thereby creating 'ridges' and 'valleys' in the total intensity field. The location of the fault would, then, be indicated by the 'valley' structures. Also, the interfaces between magnetic and non-magnetic geological formations brought in contact by tectonic action are evident by abrupt lateral changes in the intensity of the magnetic field. As a consequence, tectonic processes may result in elongate discontinuities (lineaments) in the anomalous magnetic field, which should be collocated and correlated with fault zones. It is not difficult to see that this may well be the case for the anomalies associated with the W-E oriented *HlO–Fournoi* and *RdO* ophiolitic formations, which are flanked by W-E oriented faults (Figs 11 and 14). The *HlO–Fournoi* ophiolites in particular, appear to sit directly on the horst of the Mt Adheres range and are thus tectonically delimited and completely separated from the deep-seated *Her-HdG–HdS* sources. In support of this inference, it is worth pointing out that anomalies associated with the *HlO–Fournoi* formation (Fig. 11) are conspicuously absent from Fig. 10 (anomalies generated by sources buried at depths greater than 2 km).

5.4 Deformation and crustal magmatism in Argolis peninsula: a model

An interesting aspect of our results is that active faulting with non-trivial W-E right-lateral heave has been deduced by formal inversion of earthquake focal mechanisms and is expected to operate between the Argolic and east Saronic gulfs, with particular reference to the central and southern Argolid (Argolis peninsula). The possibility of lateral-slip faulting in that area has not gone unnoticed in previous research. For instance, Van Andel *et al.* (1993) postulated the existence of two W-E left-lateral faults bracketing the north and south flanks of the Didymon–Adheres ranges and forming the homonymous horst. Given the evidence available to them at that time this fault kinematics was reasonable inference. However, our work has demonstrated not only that W-E faults with a significant horizontal slip component are expected in the area, but that they actually are *right-lateral*. This presents a small problem in that the peninsula must shift due east along dextral faults and not along sinistral faults as would intuitively be expected.

The issue can be resolved if the area of Argolis peninsula is taken to comprise a crustal block undergoing internal deformation modulated by the synthetic R-shear faulting direction, as schematically depicted in Fig. 14. According to this view, the Argolis block is approximately delimited to the NW by a putative regional

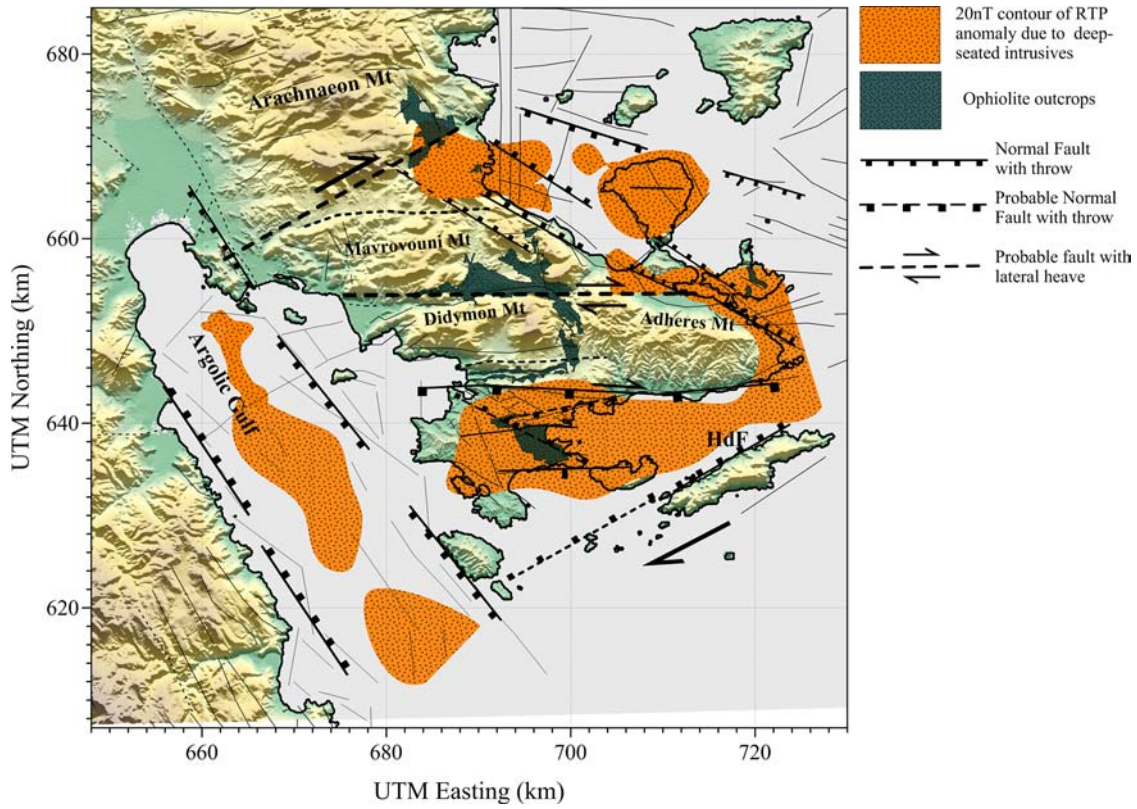

Figure 14. Tentative tectonic model for the area of Argolis peninsula. UTM northings were reduced by 3500 km so as to facilitate the display.

SW-NE shear fault zone extending along the southeastern flank of Mt Arachnaeon through to Nea Epidavros, and to the SE by the regional fault zone that forms the (graben of) Hydra Strait and is marked as HdF (Hydra Fault) in Fig. 14. In this way, the southernmost areas of Hermionis and Hydra Gulf are relatively stationary, bounded to the east by the HdF system. However, the central and south Peninsula can slide due east by right-lateral faulting, in a configuration comprising three major blocks, of which the central (Didymon–Adheres block) is moving relatively faster than the northern (Mavrovouni block) and southern (Hermionis block). The locations of the W-E faults delimiting the Didymon–Adheres block are approximately as postulated by Van Andel *et al.* (1993), but have been adjusted with respect to the W-E intrusive activity discovered herein. It is also conceivable that the two major blocks comprise ensembles of minor blocks bounded by secondary W-E lateral-slip faulting. Both major and secondary faults may be reactivated structures older than the inception of the CR, or structures inherited from the earlier stages of CR formation (Late Pliocene).

This model is consistent with the differences in the configuration of major normal faulting at the west and east coasts of the peninsula, namely the NW-SE southwesterly dipping faults of the Argolic coast versus the WNW-ESE northeasterly dipping faults of the Saronic coast. It is rather easy to see how any consequent strain differential due to disparity in the extension directions (and rates) of the Argolic and Saronic gulfs can be accommodated by the right-lateral drift. The model is also consistent with the localization of intrusive activity in certain zones of more intense W-E deformation, specifically: (i) along the Hermionis–Hydra Gulf–Hydra Strait–Cape Skillaion line, just off the southern boundary faults of the Didymon–Adheres block. (ii) Along the Kalloni–Poros line at the eastern end of the boundary separating the Didymon–Adheres and Mavrovouni blocks and, (iii) along the Palaea Epidavros–Methana line coincidentally with the northern boundary of the Mavrovouni block. Finally, the model is consistent with the anisotropic W-E geographical configuration and geomorphological characteristics of the central and southern Argolis peninsula (also see Vassilopoulou 1999, 2010). In order to exemplify this point, Fig. 14 is underlain by a shaded relief image of the topography, lit from the north.

As a concluding general comment, we note that we have found evidence of extensive, hitherto unknown and largely unsuspected syn-rift plutonic magmatism beneath the Argolid, apparently related to the Hellenic Subduction and Volcanic Arc, as well as to rifting in the CR system. This type of large-scale intrusive activity indicates a link (interaction) between deep-seated processes related to the local characteristics of the subducting slab and the deformation of the southwestwardly moving crust of the Aegean forearc. The mechanism generating the local deformation pattern postulated for Argolis peninsula is certainly part of these processes. The analysis and identification of such interactions will not be pursued herein; they will be revisited in follow-up work with the aid of additional multiparametric observational evidence.

ACKNOWLEDGEMENTS

We are indebted to Dr V. Sakkas and Dr E. Lagios (Department of Geology and Geo-environment, National and Kapodestrian University of Athens), for providing the raw output of the inversion of the magnetotelluric cross-section presented in Galanopoulos *et al.* (2005). We sincerely appreciate several astute and punctual comments by Dr D.J.W. Piper of the Geological Survey of Canada.

We also acknowledge several insightful discussions with Dr Haralambos Kranis (Department of Geology and Geo-environment, National and Kapodestrian University of Athens).

REFERENCES

Amante, C. & Eakins, B.W., 2009. ETOPO1 1 arc-minute global relief model: procedures, data sources and analysis. NOAA Technical Memorandum NESDIS NGDC-24. National Geophysical Data Center, NOAA. doi:10.7289/V5C8276M (last accessed December 2016).

Armijo, R., Meyer, B., King, G., Rigo, A. & Papanastassiou, D., 1996. Quaternary evolution of the Corinth Rift and its implications for the late Cenozoic evolution of the Aegean, *Geophys. J. Int.,* **126**(1), 11–53.

Avallone, A. *et al*., 2004. Analysis of eleven years of deformation measured by GPS in the Corinth Rift Laboratory area, *C. R. Geosci.,* **336**(4–5), 301–311.

Basili, R. *et al*., 2013. The European Database of Seismogenic Faults (EDSF) compiled in the framework of the Project SHARE. Available at: http://diss.rm.ingv.it/share-edsf/, doi:10.6092/INGV.IT-SHARE-EDSF (last accessed December 2016).

Bhattacharyya, B.K. & Leu, L.K., 1975. Spectral analysis of gravity and magnetic anomalies due to two-dimensional structures, *Geophysics,* **40**(6), 993–1013.

Billiris, H. *et al*., 1991. Geodetic determination of tectonic deformation in central Greece from 1900 to 1988, *Nature,* **350**(6314), 124–129.

Blakely, R.J., 1995. *Potential Theory in Gravity and Magnetic Applications*, Cambridge Univ. Press.

Bondar, I. & Storchak, D., 2011, Improved location procedures at the International Seismological Centre, *Geophys. J. Int.,* **186**(3), 1220–1244.

Briole, P. *et al*., 2000. Active deformation of the Corinth Rift, Greece: results from repeated Global Positioning System surveys between 1990 and 1995, *J. geophys. Res.,* **105**(B11), 25 605–25 625.

Chailas, S., Tzanis, A., Kranis, H. & Karmis, P., 2010. Compilation of a unified and homogeneous aeromagnetic map of the Greek Mainland, *Bull. geol. Soc. Greece,* **43**(4), 1919–1929.

Clarke, P.J. *et al*. 1998. Crustal strain in central Greece from repeated GPS measurements in the interval 1989–1997, *Geophys. J. Int.,* **135**(1), 195–214.

D'Alessandro, A., Papanastasiou, D. & Baskoutas, I., 2011. Hellenic Unified Seismological Network: an evaluation of its performance through SNES method, *Geophys. J. Int.,* **185**(3), 1417–1430.

Daubechies, I., 1992. *Ten Lectures on Wavelets*, CBMS Regional Conference Series in Applied Mathematics, SIAM, Philadelphia, PA.

DeMartini, P.M., Pantosti, D., Palyvos, N., Lemeille, F., McNeill, L. & Collier, R., 2004. Slip rates of the Aigion and Eliki faults from uplifted marine terraces, Corinth Gulf, Greece, *C. R. Geosci.,* **336**(4–5), 325–334.

Dietrich, V. & Gaitanakis, P., 1995. *Geological Map of Methana Peninsula (Greece)*, ETH Zürich, Switzerland.

Dotsika, E., Poutoukis, D. & Raco, B., 2010. Fluid geochemistry of the Methana Peninsula and Loutraki geothermal area, Greece, *J. Geochem. Explor.,* **104**(3), 97–104.

Doutsos, T. & Piper, D.J.W., 1990. Listric faulting, sedimentation, and morphological evolution of the Quaternary eastern Corinth rift, Greece: first stages of continental rifting, *Bull. geol. Soc. Am.*, **102**(6), 812–829

Drakatos, G., Karastathis, V., Makris, J., Papoulia, J. & Stavrakakis, G., 2005. 3D crustal structure in the neotectonic basin of the Gulf of Saronikos (Greece), *Tectonophysics,* **400**(1–4), 55–65.

Efstathiou, A., 2011. Volcanism and geothermy at the Argolis Peninsula (East Peloponnesus, Greece), *MSc thesis*, Faculty of Geology, National and Kapodistrian University of Athens.

Flotté, N., Sorel, D., Miller, C. & Tensi, J. 2005. Along strike changes in the structural evolution over a brittle detachment fault: example of the Pleistocene Corinth–Patras rift (Greece), *Tectonophysics,* **403**(1–4), 77–94.

Francalanci, L., Vougioukalakis, G.E., Perini, G. & Manetti, P., 2005. A West-East Traverse along the magmatism of the south Aegean volcanic arc in the light of volcanological, chemical and isotope data, in *The South Aegean Volcanic Arc, Present Knowledge and Future Perspectives*, pp. 65–111, eds Fytikas, M. & Vougioukalakis, G., Elsevier.

Gaitanakis, P. & Photiades, A.D., 1989. The ophiolitic units of the Argolid (Peloponnese, Greece), *Bull. geol. Soc. Greece,* **23**(1), 363–380 (in Greek with French abstract).

Gaitanakis, P. & Photiades, A., 1993. New data on the geology of Southern Argolid, *Bull. geol. Soc. Greece,* **28**(1), 247–267 (in Greek with English abstract).

Gaitanakis, P. & Photiades, A.D., 1991. Geological structure of SW Argolid, *Bull. geol. Soc. Greece,* **25**(1), 319–338 (in Greek with French abstract).

Galanopoulos, D., Sakkas, V., Kosmatos, D. & Lagios, E., 2005. Geoelectric investigation of the Hellenic subduction zone using long period magnetotelluric data, *Tectonophysics,* **409**(1–4), 73–84.

Goldsworthy, M. & Jackson, J., 2001. Migration of activity within normal fault systems: examples from the Quaternary of mainland Greece, *J. Struct. Geol.,* **23**(2–3), 489–506.

Grove, T.L., Chatterjee, N., Parman, S.W. & Médard, E., 2006. The influence of H_2O on mantle wedge melting, *Earth planet. Sci. Lett.,* **29**(1–2), 74–89.

Hardebeck, J.L. & Hauksson, E., 2001. Stress orientations obtained from Earthquake focal mechanisms: what are appropriate uncertainty estimates?, *Bull. seism. Soc. Am.,* **91**(2), 250–262.

Hardebeck, J.L. & Michael, A.J., 2006. Damped regional-scale stress inversions: methodology and examples for southern California and the Coalinga aftershock sequence, *J. geophys. Res.,* **111**, B11310, doi:10.1029/2005JB004144.

Hatzfeld, D. *et al*., 1989. The Hellenic subduction beneath the Peloponnesus: first results of a microearthquake study, *Earth planet. Sci. Lett.,* **93**(2), 283–291.

Hatzfeld, D., Besnard, M., Makropoulos, K. & Hatzidimitriou, P., 1993. Microearthquake seismicity and fault-plane solutions in the southern Aegean and its geodynanic implications, *Geophys. J. Int.,* **115**(3), 799–818.

Kahle, H.-G., Cocard, M., Yannick, P., Geiger, A., Reilinger, R., Barka, A. & Veis, G., 2000. GPS-derived strain rate field within the boundary zones of the Eurasian, African, and Arabian Plates, *J. geophys. Res.,* **105**(B10), 23 353–23 370.

Kaplanis, A., Koukouvelas, I., Xypolias, P. & Kokkalas, S., 2013. Kinematics and Ophiolite obduction in the Gerania and Helicon Mountains, central Greece, *Tectonophysics,* **595–596,** 215–234.

Kiratzi, A. & Louvari, E., 2003. Focal mechanisms of shallow earthquakes in the Aegean Sea and the surrounding lands determined by waveform modelling: a new database, *J. Geodyn.,* **36**(1–2), 251–274.

Kokkalas, S. & Aydin, A., 2013. Is there a link between faulting and magmatism in the south-central Aegean Sea?, *Geol. Mag.* **150**(2), 193–224.

Konstantinou, K.I., Melis, N.S. & Boukouras, K., 2010. Routine regional moment tensor inversion for earthquakes in the Greek region: The National Observatory of Athens (NOA) database (2001–2006), *Seismol. Res. Lett.,* **81,** 750–760.

Kotopouli, C.N., Pe-Piper, G. & Piper, D.J.W., 2000. Petrology and evolution of the Hercynian Pieria Granitoid Complex (Thessaly, Greece): paleogeographic and geodynamic implications, *Lithos,* **50**(1–3), 137–152.

Kranis, H.D., 1999. Neotectonic activity of fault zones in Lokris, central-eastern mainland Greece, *PhD thesis*, Faculty of Geology, National and Kapodistrian University of Athens, (GAIA publ. No. 10), 234 pp.

Leeder, M.R. *et al*., 2012. A 'Great Deepening': chronology of rift climax, Corinth rift, Greece, *Geology,* **40**(11), 999–1002.

Manthilake, G., Bolfan-Casanova, N., Novella, D., Mookherjee, M. & Andrault, D., 2016. Dehydration of chlorite explains anomalously high electrical conductivity in the mantle wedges, *Sci. Adv.,* **2**(5), doi:10.1126/sciadv.1501631.

Martínez-Garzón, P., Kwiatek, G., Ickrath, M. & Bohnhoff, M., 2014. MSATSI: a MATLAB Package for stress inversion combining solid classic methodology, a new simplified user-handling and a visualization tool, *Seismol. Res. Lett.*, **85**(4), doi:10.1785/0220130189.

McClusky, S.C. *et al*., 2000. Global positioning system constraints on plate kinematics and dynamics in the eastern Mediterranean and Caucasus, *J. geophys. Res.,* **105**(B3), 5695–5719.

McNeill, L.C. *et al*., 2005. Active faulting within the offshore western Gulf of Corinth, Greece: implications for models of continental rift deformation, *Geology,* **33**(4), 241–244.
Michael, A.J., 1984. Determination of stress from slip data: faults and folds, *J. geophys. Res.,* **89**(B13), 11 517–11 526.
Michael, A.J., 1987. Use of focal mechanisms to determine stress: a control study, *J. geophys. Res.,* **92**(B1), 357–368.
Michael, A.J., 1991. Spatial variations in stress within the 1987 Whittier Narrows, California, aftershock sequence: new techniques and results, *J. geophys. Res.,* **96**(B4), 6303–6319.
Mitropoulos, P., 1987. Primary allanite in andesitic rocks from the Poros Volcano, Greece, *Mineral. Mag.,* **51**(62), 601–604.
Papadeas, G., 1989. *Geological Map of Attica*, Institute of Geological and Mineral Exploration (IGME), Athens, Greece.
Papanikolaou, D., Lykousis, V., Chronis, G. & Pavlakis, P., 1988. A comparative study of neotectonic basins across the Hellenic arc: the Messiniakos, Argolikos, Saronikos and Southern Evoikos Gulfs, *Basin Res.,* **1**(3), 167–176.
Papanikolaou, D. & Lozios, S., 1990. Comparative neotectonic structure of high (Korinthia-Beotia) and low rate (Attica-Cyclades) activity, *Bull. geol. Soc. Greece,* **26,** 47–66 (in Greek with English abstract).
Papazachos, B.C., Karakostas, V.E., Papazachos, C.B. & Scordilis, E.M., 2000. The geometry of the Wadati–Benioff zone and lithospheric kinematics in the Hellenic arc, *Tectonophysics,* **319**(4), 275–300.
Pawlowski, R.S. & Hansen, R.O. 1990. Gravity anomaly separation by Wiener filtering, *Geophysics,* **55**(5), 539–548.
Pe-Piper, G., 2000. Origin of S-type granites coeval with I-type granites in the Hellenic subduction system, Miocene of Naxos, Greece, *Eur. J. Mineral.,* **12**(4), 859–875.
Pe-Piper, G. & Piper, D.J.W., 2002. *The Igneous Rocks of Greece: Anatomy of an Orogen*, Bornträger, Berlin.
Pe-Piper, G. & Piper, D.J.W., 2013. The effect of changing regional tectonics on an arc volcano: Methana, Greece, *J. Volc. Geotherm. Res.,* **260,** 146–163.
Peter, Y., Kahle, H., Cocard, M., Veis, G., Felekis, S. & Paradissis, D., 1998. Establishment of a continuous GPS network across the Kephalonia Fault Zone, Ionian islands, Greece, *Tectonophysics,* **294**(3–4), 253–260.
Pham, V.N., Bernard, P., Boyer, D., Chouliaras, G., Le Mouël, J.L. & Stavrakakis, G.N., 2000. Electrical conductivity and crustal structure beneath the central Hellenides around the Gulf of Corinth (Greece) and their relationship with the seismotectonics, *Geophys. J. Int.,* **142**(3), 948–969.
Photiades, A.D. & Keay, S., 2000. Mid-Late Jurassic granodiorite basement in southern Argolis Peninsula (Greece): tectonostratigraphic implications, in *Proceedings of the third International Conference on the Geology of the Eastern Mediterranean*, pp. 233–239, eds Panayides, I., Xenophontos, C. & Malpas, J. , Geological Survey Department, Cyprus.
Rigo, A., Lyon-Caen, H., Armijo, R., Deschamps, A., Hatzfeld, D., Makropoulos, K., Papadimitriou, P. & Kassaras, I., 1996. A microseismic study in the western part of the Gulf of Corinth (Greece): implications for large-scale normal faulting mechanisms, *Geophys. J. Int.,* **126**(3), 663–688.
Ritsema, A., 1974. The earthquake mechanics of the Balkan region, Royal Netherlands Meteorological Institute, De Bilt, *Sci. Rep.,* **74**(4), 1–36.
Sachpazi, M., Clement, C., Laigle, M., Hirn, A. & Roussos, N., 2003. Rift structure, evolution, and earthquakes in the Gulf of Corinth, from reflection seismic images, *Earth planet. Sci. Lett.,* **216**(3), 243–257.
Sachpazi, M. *et al*. 2007. Moho topography under central Greece and its compensation by Pn time-terms for the accurate location of hypocenters: the example of the Gulf of Corinth 1995 Aigion earthquake, *Tectonophysics,* **440**(1–4), 53–65.
Sachpazi, M. *et al*., 2016. Segmented Hellenic slab rollback driving Aegean deformation and seismicity, *Geophys. Res. Lett.,* **43**(2), 651–658.
Skourtsos, E. & Kranis, H., 2009. Structure and evolution of the western Corinth Rift, through new field data from the Northern Peloponnesus, in *Extending a Continent: Architecture, Rheology and Heat Budget*, Vol. 321, pp. 119–138, eds Ring, U. & Wernicke, B. The Geological Society, London, Special Publications.
Smet, I., 2014. Spatial and temporal petrological-geochemical variations in the volcanic rocks of the Saronic Gulf (West Aegean arc, Greece): influence of local geodynamic parameters on magma genesis, *PhD thesis*, Ghent University, Belgium, 349 pp.
Spector, A. & Grant, F.S., 1970. Statistical models for interpreting aeromagnetic data, *Geophysics,* **35**(2), 293–302.
Sperner, B., Müller, B., Heidbach, O., Delvaux, D., Reinecker, J. & Fuchs, K., 2003. Tectonic stress in the Earth's crust: advances in the World Stress Map project, in *New Insights in Structural Interpretation and Modelling*, Vol. 212, pp. 101–116, ed. Nieuwland, D.A., The Geological Society, London, Special Publications.
Stefatos, A., Papatheodorou, G., Ferentinos, G., Leeder, M. & Collier, R., 2002. Seismic reflection imaging of active offshore faults in the Gulf of Corinth: their seismotectonic significance, *Basin Res.,* **14**(4), 487–502.
Suckale, J., Rondenay, S., Sachpazi, M., Charalampakis, M., Hosa, A. & Royden, L.H., 2009. High-resolution seismic imaging of the western Hellenic subduction zone using teleseismic scattered waves, *Geophys. J. Int.,* **178**(2), 775–791.
Taktikos, S., 2001. *Heat Flow—Underground Temperatures of Greece*; *Set of Two Volumes and 12 Maps*, Institute of Geological and Mineral Exploration (IGME), Athens, Greece (in Greek).
Tselentis, G.-A., 1991. An attempt to define Curie point depths in Greece from aeromagnetic and heat flow data, *Pageoph,* **136**(1), 87–101.
Tzanis, A., Kranis, H. & Chailas, S., 2010. An investigation of the active tectonics in central-eastern mainland Greece with imaging and decomposition of topographic and aeromagnetic data, *J. Geodyn.,* **49**(2), 55–67.
Van Andel, T.H., Perissoratis, C. & Rondoyanni, T., 1993. Quaternary tectonics of the Argolikos Gulf and adjacent basins, Greece, *J. geol. Soc.,* **150**(3), 529–539.
Vassilopoulou, S., 1999. Geodynamics of the argolis peninsula with G.I.S development and use of remote sensing data, *PhD thesis*, Faculty of Geology, National and Kapodistrian University of Athens (in Greek).
Vassilopoulou, S., 2010. Morphotectonic analysis of Southern Argolis Peninsula (Greece) based on ground and satellite data by GIS development, *Bull. geol. Soc. Greece,* **43**(1), 516–525.
Wessel, P., Smith, W.H.F., Scharroo, R., Luis, J.F. & Wobbe, F., 2013. Generic mapping tools: improved version released, *EOS, Trans. Am. geophys. Un.,* **94**(45), 409–410.
Westaway, R., 2002. The Quaternary evolution of the Gulf of Corinth, central Greece: coupling between surface processes and flow in the lower continental crust, *Tectonophysics,* **348**(4), 269–318.
Xia, J., Sprowl, D.R. & Adkins-Heljeson, D., 1993. Correction of topographic distortions in potential-field data: a fast and accurate approach, *Geophysics,* **58**(4), 515–523.
Zoback, M.D. & Zoback, M.L., 1991. Tectonic stress field of North America and relative plate motions, in Neotectonics of North America, pp. 339–366, eds Slemmons, D.B., Engdahl, E.R., Zoback, M.D. & Blackwell, D.D. Geological Society of America, Boulder.
Zoback, M.L. & Zoback, M.D., 1989. Tectonic stress field of the conterminous United States, *Mem. Geol. Soc. Am.,* **172,** 523–539.

APPENDIX: WAVELET FILTERS FOR EFFECTIVE SEPARATION OF POTENTIAL FIELD ANOMALIES

Magnetic anomaly separation directly relevant to the depth of the sources can be based on a wavenumber domain Wiener filtering approach, as for instance in the scheme proposed by Pawlowski & Hansen (1990). This method uses the ensemble power spectrum $P_r(k)$ to represent the signal power and defines 1-D zero-phase Wiener filters of the form

$$G_{PH}(k) = \frac{A \cdot k^2 \cdot e^{-2kZ_1}}{P_r(k)}, \tag{A1}$$

where the nominator comprises the response of a depth-limited source ensemble whose ceiling is buried at a depth of Z_1 km, as expressed by Spector & Grant (1970). The 1-D filters can be subsequently mapped onto zero-phase matrix (2-D) filters and applied to the data in the Fourier domain. A similar approach implements the response of depth-limited ensembles whose ceilings and floors are buried at depths $Z_1 > Z_2$, respectively. Blakely (1995) has shown that this is

$$H(k) = Be^{-2kZ_2}\left(1 - e^{-k(Z_1-Z_2)}\right)^2,$$

so that the corresponding Wiener filter would be

$$G_B(k) = \frac{Be^{-2kZ_2}\left(1 - e^{-k(Z_1-Z_2)}\right)^2}{P_r(k)} \tag{A2}$$

Clearly, $G_{\rm PH}$ and $G_{\rm B}$ comprise classes of bandpass filters designed to isolate the response of depth-limited ensembles on the basis of information extracted from the radially averaged power spectrum. These approaches have a cardinal advantage in that they guide the separation of anomalies on the basis of structural information directly recoverable from the data. However, they are not effective as can be easily demonstrated.

In the scenario of Fig. A1(a), the analysis seeks to separate an ensemble of sources (target) known to be buried between $Z_1 = 3.8$ km and $Z_2 = 1.8$ km, when the Nyquist wavenumber is 4π cycles km^{-1}, meaning that the input data have a grid spacing of 0.25 km as with the data treated herein (Section 4). Logic dictates that the target ensemble would be delimited by the wavenumber corresponding to the peak of a Spector and Grant (S&G) response computed for $Z_1 = 3.8$ km, which is $k_1 = 0.2592$ cycles km^{-1}, and the wavenumber corresponding to the peak of an S&G response computed for $Z_2 = 1.8$ km, which is $k_2 = 0.5576$ cycles km^{-1}: the argument assumes that the target ensemble is succeeded by a depth-limited concentration of sources but this is inconsequential to the analysis. The peak wavenumber of the Blakely response is $k_0 = 0.3762$ cycles km^{-1}, which is neatly situated at approximately midways between k_1 and k_2. Clearly, $G_{\rm PH}(k_1)$ and $G_{\rm PH}(k_2)$ are neither efficient nor effective: due to their bell-shaped form and blunt roll-off, they significantly attenuate proper spectral content of the target ensemble while assimilating shorter than k_1 or longer than k_2 spectral content, that is from depths below the floor or above the ceiling of the ensemble. Equally clearly, $G_{\rm B}(Z_1, Z_2)$ fares much better although not very well. To begin with, it attenuates some spectral content of the target ensemble: the amplitudes at wavenumbers k_1 and k_2 are reduced by 12 per cent and 16 per cent, respectively, which it certainly not excessive but also not desirable. Conversely, it admits information from spectral content outside of the target ensemble: 77 per cent and 80 per cent of the spectral components at $k = 0.2238 < k_1$ and $k = 0.604 > k_2$ are admitted, while the low roll-off rates ensure that a significant amount of outside information will be filtered-in. These examples make evident that efficient recovery of the spectral signatures of depth-limited sources requires filters with flat as possible passbands for $k \in [k_1, k_2]$ and sharp as possible roll-off bands for $k \notin [k_1, k_2]$. The problem can be addressed with conventional IIR or FIR filters. These, however, are complex in the Fourier domain and have to be applied in the forward and reverse spatial sense in order to avoid translations in the location of anomalies. This is not a problem in itself but such filters are also associated with ripple structure whose suppression is linked to the width of the passband, the roll-off rate and the magnitude of phase shifts, particularly when the passband is narrow and/or squeezed at the short wavenumber realm: their design is not always straightforward or optimal.

In response to the difficulties described above, we introduce a set of filters with all the desirable characteristics. Specifically, these filters are (i) *real* in the Fourier plane (no phase shifts), (ii) have perfectly flat passbands (no ripples), (iii) are automatically localizable with respect to any interval $[k_1, k_2]$ and, (iv) exhibit optimally sharp roll-off bands so as to suppress all information outside the span of the target ensemble. The filters will be described at an elementary (introductory) level, with due rigour reserved for a follow-up, more specialized presentation.

Consider a smooth and *admissible* profile $W(r)$ compactly supported on $[-2, -1/2] \cup [1/2, 2]$. This allows for particularly efficient localization and has been used for the development of *Meyer* wavelets. W is a Meyer Window (MW) when it has the form (see Daubechies 1992, pp. 115–120),

$$W(r) = \begin{cases} \cos\left[\frac{\pi}{2} w(5-6r)\right] & \frac{2}{3} \le r \le \frac{5}{6} \\ 1 & \frac{5}{6} \le r \le \frac{4}{3} \\ \cos\left[\frac{\pi}{2} w(3r-4)\right] & \frac{4}{3} \le r \le \frac{5}{3} \\ 0 & \text{otherwise} \end{cases}, \tag{A3}$$

with $w(x)$ satisfying

$$w(x) = \begin{cases} 0 & x \le 0 \\ 1 & x \ge 1 \end{cases}, \qquad w(t) + w(1-x) = 1, \quad x \in \mathbb{R}. \tag{A4}$$

In order to obtain smooth W, it is necessary to use smoother $w(x)$. Common forms are the polynomials $w(x) = 3x^2 - 2x^3$ or $w(x) = 5x^3 - 5x^4 + x^5$ in $[0, 1]$, such that $w \in C^1(\mathbb{R})$ and $w \in C^2(\mathbb{R})$, respectively. It is also possible to obtain arbitrarily smooth W when

$$w(x) \begin{cases} 0 & x \le 0 \\ \frac{s(x-1)}{s(x-1)+s(x)} & 0 < x < 1 \\ 1 & x \ge 1 \end{cases},$$

$$s(x) = \exp\left(-\frac{1}{(1+x)^2} - \frac{1}{(1-x)^2}\right) \tag{A5}$$

The MW can be localized and scaled with respect to a particular (target) wavenumber k_0 by letting $r = k/k_0$. In turn, k_0 can be specified manually, or be determined objectively on the basis of simulations of the radial spectrum with models obeying the Spector & Grant (1970), or Blakely (1995) formalisms.

An example of a 1-D MW profile constructed with the aid of the Blakely response is shown in Fig. A1(a). As discussed above, the peak of the Blakely response corresponds to $k_0 = 0.3762$ cycles km^{-1}. The MW is automatically scaled around this particular k_0, as indicated with the thick solid line. In obvious contrast to the ensemble responses (or G_{PH} and G_B filters), the MW has a perfectly flat passband and very sharp roll-off so that it will only admit information pertaining to a rather narrow band around k_0; its output will *certainly not* be contaminated by irrelevant contributions from deeper or shallower sources. Nevertheless, it is equally obvious that in this case, the passband of the MW does not span the entire $[k_1, k_2]$ interval: it is certainly more localized. Conversely, there may be instances in which the desired passband is narrow enough for the window to transcend $[k_1, k_2]$ so as to admit unwanted information.

Due to the limitations stated above, the MW window will not be used in the present analysis; rather, it was presented as an intermediary by which to introduce a more useful construct that remedies its limitations while retaining its advantages. This construct, henceforth to be dubbed '*Extended Meyer Window*' or EMW, can be

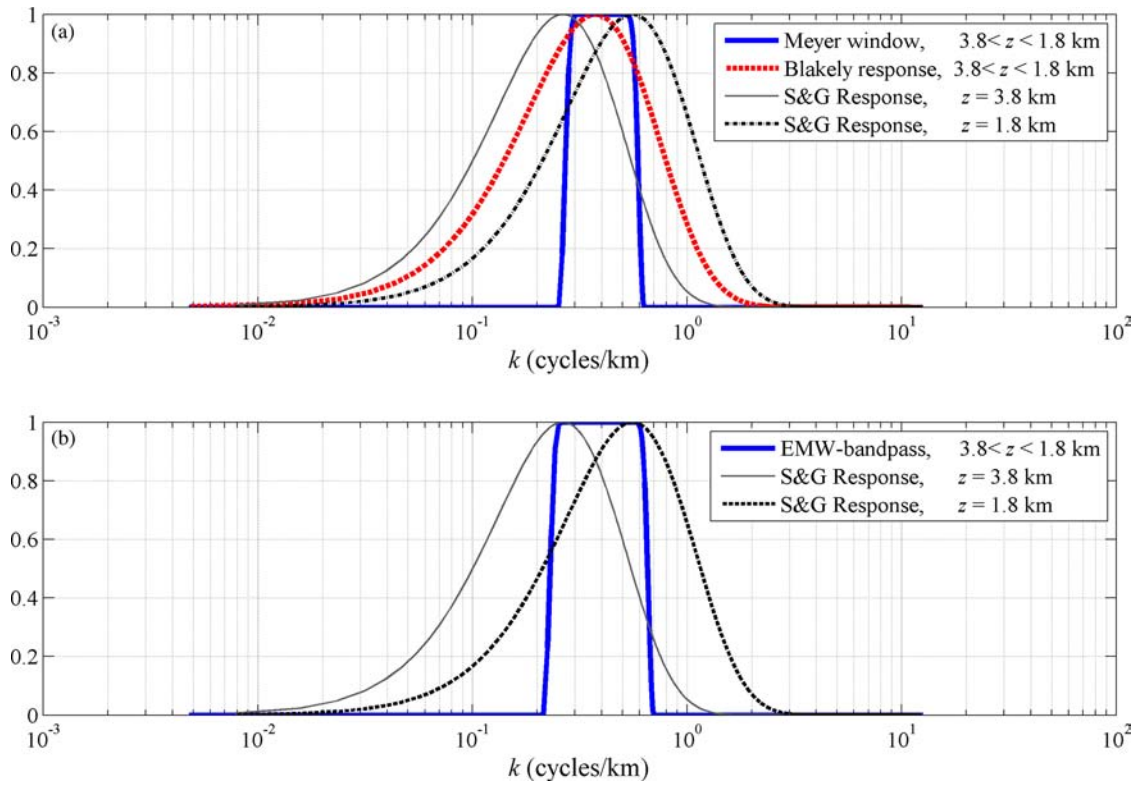

Figure A1. Different bandpass filters intended to isolate a magnetic source ensemble buried between 3.8 and 1.8 km. (a) Comparison of Wiener filters based on the Spector and Grant (S&G) and Blakely responses, to a Meyer Window filter localized (tuned) with respect to the peak of the Blakely response. (b) Realization of an Extended Meyer Window filter localized with respect to the peaks of the S&G responses for $Z_1 = 3.8$ and $Z_2 = 1.8$ km (see the text for details).

defined as follows:

$$F(r) = \begin{cases} \cos\left[\frac{\pi}{2} w(5-6r)\right], & \frac{2}{3} \le r \le \frac{5}{6} \;:\; r = \frac{5}{6}\frac{k}{k_1} \;\leftrightarrow\; k \le k_1 \\ 1, & \frac{5}{6} < r < \frac{4}{3} \;:\; r = \frac{k}{\beta(k)} \;\leftrightarrow\; k_1 < k < k_2 \\ \cos\left[\frac{\pi}{2} w(3r-4)\right], & \frac{4}{3} \le r \le \frac{5}{3} \;:\; r = \frac{4}{3}\frac{k}{k_2} \;\leftrightarrow\; k_2 \le k \\ 0 & \text{otherwise} \end{cases} \tag{A6}$$

As can be seen in eq. (A6), the terminus of the low-wavenumber cut-off is moved to k_1 by stretching (dilating or contracting) the passband so that $r(k) \approx 5/6$ when $k \approx k_1$. Likewise, the origin of the high-wavenumber cut-off is moved to k_2 by stretching the passband so that $r(k) \approx 4/3$ when $k \approx k_2$. The passband is unity for all $r \in (5/6, 4/3)$ or, equivalently, $k \in (k_1, k_2)$. To achieve this (and compensate for stretching, a normalizing function $\beta(k)$ is necessary, such that

$$\frac{5}{6}\frac{k}{k_1} < \frac{k}{\beta(k)} < \frac{4}{3}\frac{k}{k_2} \quad \Rightarrow \quad \frac{6}{5}k_1 > \beta(k) > \frac{3}{4}k_2;$$

$\beta(k)$ may be determined by interpolation, although in practice this is not required (see below). The EMW is *compactly supported* on $[-2, -1/2] \cup [1/2, 2]$ and can be shown to comprise an admissible profile: it is a filter *and* a wavelet at the same time. Formal proof of this claim is relatively easy and based on the same procedure proving that $W(r)$ is admissible (e.g. Daubechies 1992). It will not be given herein for the sake of brevity but is reserved for a follow-up, more specialized and detailed presentation. Conversely, empirical (numerical) verification is rather straightforward: by taking the inverse Fourier transform $f(x)$ of *any* realization of $F(k)$, it is easy to determine that the *admissibility condition* $\Sigma_x f(x) = 0$, is *always* upheld.

An equivalent definition of the EMW, more useful for programming, is:

$$F(k) = \begin{cases} \cos\left[\frac{\pi}{2} w(5-5\frac{k}{k_1})\right], & \frac{2}{3} \le \frac{5}{6}\frac{k}{k_1} \le \frac{5}{6} \\ 1, & k_2 < k < k_1 \\ \cos\left[\frac{\pi}{2} w(4\frac{k}{k_2}-4)\right], & \frac{4}{3} \le \frac{4}{3}\frac{k}{k_2} \le \frac{5}{3} \\ 0, & \text{otherwise} \end{cases} \tag{A7}$$

Eq. (A7) indicates that EMW filters can be converted to low pass by letting

$$F_l(k) = \begin{cases} 1 & k < k_2 \\ \cos\left[\frac{\pi}{2} w(4\frac{k}{k_2}-4)\right] & \frac{4}{3} \le \frac{4}{3}\frac{k}{k_2} \le \frac{5}{3} \\ 0 & \text{otherwise} \end{cases} \tag{A8}$$

or to high pass by letting

$$F_h(r) = \begin{cases} \cos\left[\frac{\pi}{2} w(5-5\frac{k}{k_1})\right] & \frac{2}{3} \le \frac{5}{6}\frac{k}{k_1} \le \frac{5}{6} \\ 1 & k_1 < k \\ 0 & \text{otherwise} \end{cases} \tag{A9}$$

Fig. A1(b) illustrates an EMW bandpass profile appropriate for the analysis presented herein; it is designed to separate a depth-limited ensemble buried between $Z_1 = 3.8$ km ($k_1 = 0.2592$ cycles km^{-1}) and $Z_2 = 1.8$ km ($k_2 = 0.5576$ cycles km^{-1}), where the wavenumbers correspond to the peaks of the respective depth-limited S&G responses. The EMW filter is perfectly flat for $k \in (k_1, k_2)$ and

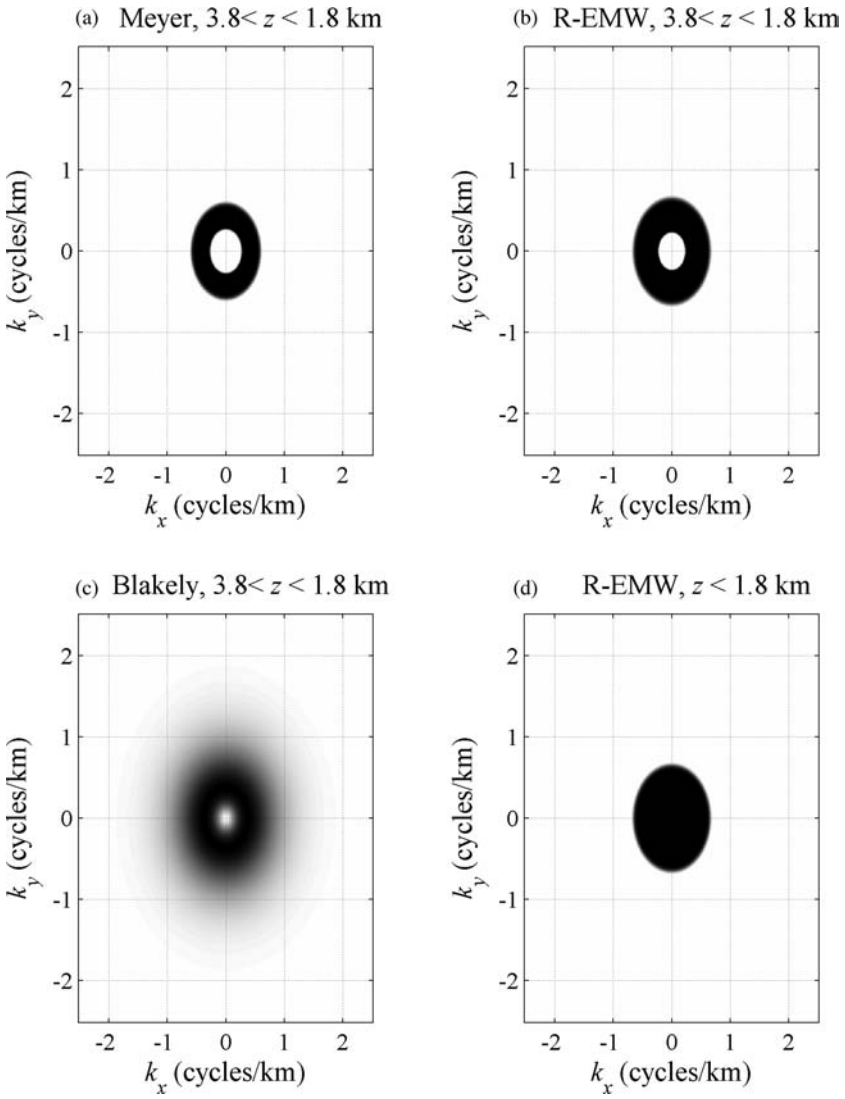

Figure A2. 2-D bandpass and low-pass filters intended to isolate magnetic anomalies generated by magnetic sources buried between $Z_1 = 3.8$ km and $Z_2 = 1.8$ km. (a) Bandpass Radial Meyer Window comprising 2-D extension of the Meyer Window profile shown in Fig. A1(a). (b) Bandpass Radial Extended Meyer Window comprising D extension of the bandpass EMW shown in Fig. A1(b). (c) Bandpass Wiener filter based on the Blakely response, 2-D extension of the Blakely response shown in Fig. A1(a). (d) Low-pass Radial Extended Meyer Window with cutoff at $|k_2| = 0.5576$, designed to isolate sources buried at depths greater than Z_2.

exhibits sharp roll-off, identical to that of the Meyer window; the left roll-off band terminates at exactly k_1 (low cut-off wavenumber) and the right roll-off band commences at exactly k_2 (high cut-off wavenumber). On using this filter, only spectral content relevant to the target ensemble can be admitted, without loss of information or unwanted side-effects (ripples, phase shifts, Gibbs effects, etc.).

The 1-D profiles (A2), (A3) and (A6)–(A9) can readily be expanded to two dimensions. At each position (k_x, k_y) of the Fourier plane, the modulus $|k| = \sqrt{k_x^2 + k_y^2}$ represents a radial wavenumber. Thus, if $|\mathbf{k}|$ is the matrix of radial wavenumbers, it is easy to generate a 2-D radial Meyer window scaled and localized with respect to some $|k_0|$, by letting $\mathbf{r} = |\mathbf{k}|/|k_0|$, with $|k_0|$ still determinable as before, on the basis of the radially averaged power spectrum ($k_0 \equiv |k_0|$). Likewise, it is possible to construct 2-D radial EMW (REMW) filters. For instance, the bandpass REMW filter is

$$F(\mathbf{k}) = \begin{cases} \cos\left[\frac{\pi}{2} w(5 - 5\frac{\mathbf{k}}{k_1})\right], & \frac{2}{3} \le \frac{5}{6}\frac{\mathbf{k}}{k_1} \le \frac{5}{6} \\ 1, & k_1 < \mathbf{k} < k_2 \\ \cos\left[\frac{\pi}{2} w(3\frac{\mathbf{k}}{k_2} - 4)\right], & \frac{2}{3} \le \frac{4}{3}\frac{\mathbf{k}}{k_2} \le \frac{5}{3} \\ 0, & \text{otherwise} \end{cases}$$

with $k_1 \equiv |k_1|$ and $k_2 \equiv |k_2|$ again determinable through the radially averaged power spectrum.

A number of 2-D filters are illustrated in Fig. A2. Specifically, Fig. A2(a) shows a radial Meyer window localized around

$k_0 = 0.3762$ cycles km^{-1}; it comprises the 2-D extension of the Meyer window depicted in Fig. A1(a). Fig. A2(b) illustrates a bandpass REMW filter comprising the 2-D extension of the bandpass EMW shown in Fig. A1(b); it is designed to exactly separate a depth-limited ensemble buried between $Z_1 = 3.8$ km, ($k_1 = 0.2592$ cycles km^{-1}) and $Z_2 = 1.8$ km ($k_2 = 0.5576$ cycles km^{-1}). The differences in the passband of the radial MW and EMW filters are rather apparent. In order to facilitate comparisons, as well as for the sake of completeness, Fig. A2(c) illustrates a 2-D extension of the corresponding bandpass Wiener filter based on the Blakely response (see Fig. A1a). Finally, Fig. A2(d) illustrates a low-pass REMW filter designed to suppress information from all depths greater than $Z_2 = 1.8$ km ($|k_2| = 0.5576$ cycles km^{-1}). A high-pass REMW filter is an exact complement of the low-pass variant so that examples are not shown for brevity.